

# Structure of an integrin with an $\alpha$ I domain, complement receptor type 4

Can Xie<sup>1</sup>, Jianghai Zhu<sup>1</sup>, Xing Chen,  
Lizhi Mi, Noritaka Nishida<sup>2</sup> and  
Timothy A Springer\*

Department of Pathology, Harvard Medical School, Immune Disease  
Institute and Children's Hospital, Boston, MA, USA

We report the structure of an integrin with an  $\alpha$ I domain,  $\alpha_X\beta_2$ , the complement receptor type 4. It was earlier expected that a fixed orientation between the  $\alpha$ I domain and the  $\beta$ -propeller domain in which it is inserted would be required for allosteric signal transmission. However, the  $\alpha$ I domain is highly flexible, enabling two  $\beta$ I domain conformational states to couple to three  $\alpha$ I domain states, and greater accessibility for ligand recognition. Although  $\alpha_X\beta_2$  is bent similarly to integrins that lack  $\alpha$ I domains, the terminal domains of the  $\alpha$ - and  $\beta$ -legs, calf-2 and  $\beta$ -tail, are oriented differently than in  $\alpha$ I-less integrins. Linkers extending to the transmembrane domains are unstructured. Previous mutations in the  $\beta_2$ -tail domain support the importance of extension, rather than a deadbolt, in integrin activation. The locations of further activating mutations and antibody epitopes show the critical role of extension, and conversion from the closed to the open headpiece conformation, in integrin activation. Differences among 10 molecules in crystal lattices provide unprecedented information on interdomain flexibility important for modelling integrin extension and activation.

The EMBO Journal (2010) 29, 666–679. doi:10.1038/emboj.2009.367; Published online 24 December 2009

Subject Categories: cell & tissue architecture; structural biology  
Keywords:  $\alpha$ I domain; integrin; structure

## Introduction

Integrins are  $\alpha\beta$  heterodimeric adhesion receptors that transmit signals bidirectionally across the plasma membrane and link ligand binding to force transmission by the cytoskeleton (Springer and Wang, 2004; Luo *et al*, 2007). Four domains in the  $\alpha$ -subunit and eight in the  $\beta$ -subunit are conserved in the ectodomain of all metazoan integrins. Additionally, an  $\alpha$ I domain is inserted in the  $\alpha$ -subunit of 9 of 18 vertebrate integrins.  $\alpha$ I domains are a late integrin evolutionary specialization found only in chordata, and have ligand-binding function when present. Ligand-binding affinity of the  $\alpha$ I

domain is allosterically regulated by its homologue in the  $\beta$ -subunit, the  $\beta$ I domain. An invariant Glu residue, located a few residues after the C-terminal  $\alpha$ 7-helix of the  $\alpha$ I domain, is postulated to act as an 'intrinsic ligand', which when bound to the active  $\beta$ I domain relays activation to the  $\alpha$ I domain.

Integrin  $\alpha_X\beta_2$ , the complement receptor type 4 (CR4), is important for phagocytosis of particles opsonized with the complement product iC3b.  $\alpha_X\beta_2$  also marks dendritic cells, and functions as a danger receptor for fibrinogen and denatured or cleaved proteins (Vorup-Jensen *et al*, 2005). Deficiency of  $\alpha_X\beta_2$  and sister  $\beta_2$  integrins causes life-threatening bacterial infections. Ligands are recognized by an inserted (I) domain in the  $\alpha_X$ -subunit.

Integrins can be classified into two main subfamilies, distinguished by the presence or absence of an  $\alpha$ I domain. Structural information to date is limited to ectodomains of two integrins that lack  $\alpha$ I domains ( $\alpha$ I-less integrins),  $\alpha_V\beta_3$  (Xiong *et al*, 2001, 2002) and  $\alpha_{IIb}\beta_3$  (Xiao *et al*, 2004; Springer *et al*, 2008; Zhu *et al*, 2008), and to small fragments of  $\alpha$ I integrins, that is the isolated  $\alpha$ I domain (Springer and Wang, 2004; Luo *et al*, 2007) and  $\beta_2$ -leg fragments (Beglova *et al*, 2002; Shi *et al*, 2007).

An enduring mystery is how allostery is transmitted between the  $\alpha$ I and the  $\beta$ I domains. A specific relay mechanism involving an  $\alpha$ I domain C-terminal  $\alpha$ -helix that slides axially has been proposed (Huth *et al*, 2000; Alonso *et al*, 2002; Yang *et al*, 2004). Furthermore, it has been proposed that the  $\alpha$ I domain should be rigidly connected to other domains, because otherwise a change in interdomain orientation could replace  $\alpha$ -helix sliding (Nishida *et al*, 2006). However, this proposed rigid connection raises the question of how two known conformational states of  $\beta$ I domains (Xiao *et al*, 2004) could couple to three known states of  $\alpha$ I domains (Shimaoka *et al*, 2003; Jin *et al*, 2004).

Here, we report the crystal structure of a complete  $\alpha$ I domain integrin ectodomain. This  $\alpha$ I integrin,  $\alpha_X\beta_2$ , is in a bent, resting state, which differs significantly from that of known  $\alpha$ I-less integrin structures. The  $\alpha$ I domain is in the inactive conformation, consistent with the overall latent conformation of the ectodomain. Contrary to earlier expectation, the  $\alpha$ I domain shows surprising flexibility. This flexibility has important implications for  $\alpha$ I domain integrin function. The structure further reveals the relationships between the  $\alpha$ I domain and other domains within an intact integrin ectodomain, and other unique features relevant to integrin activation and function.

## Results and discussion

### The crystal structures and their qualities

Crystals of  $\alpha_X\beta_2$  were obtained in three lattices denoted A, B, and C (Table I). Molecular replacement using integrin  $\alpha_{IIb}\beta_3$  and  $\alpha_V\beta_3$  structures as search models failed to yield solutions. Initial phases were obtained using Ta SAD data from a crystal soaked with tantalum bromide cluster

\*Corresponding author. Department of Pathology, Program in Cellular and Molecular Medicine, Children's Hospital, 3 Blackfan Circle, Boston, MA 02115, USA. Tel.: +1 617 713 8200; Fax: +1 617 713 8232; E-mail: springer@idi.harvard.edu

<sup>1</sup>These authors contributed equally to this work

<sup>2</sup>Present address: Graduate School of Pharmaceutical Sciences, The University of Tokyo, Hongo, Bunkyo-ku, Tokyo 113-0033, Japan

Received: 18 August 2009; accepted: 5 November 2009; published online: 24 December 2009

**Table I** X-ray diffraction data<sup>a</sup>

Data set	Se MAD (Å) <sup>b</sup>			Se MAD (C)		
	Peak	Inflection	Remote	Peak	Inflection	Remote
Space group	P2 <sub>1</sub> 2 <sub>1</sub> 2 <sub>1</sub>			I2 <sub>1</sub> 2 <sub>1</sub> 2 <sub>1</sub>		
<i>Unit cell</i>						
<i>a</i> (Å)		131.9			161.2	
<i>b</i> (Å)		162.8			166.4	
<i>c</i> (Å)		536.9			536.8	
$\alpha$ (deg)		90			90	
$\beta$ (deg)		90			90	
$\gamma$ (deg)		90			90	
Wavelength (Å)	0.97926	0.97942	0.96419	0.97926	0.97942	0.96419
Resolution (Å)	50–3.8	50–3.8	50–3.8	50–4.0	50–4.0	50–4.0
Completeness (%)	99.5 (99.4)	99.5 (99.4)	99.6 (99.5)	99.3 (99.5)	99.5 (99.7)	99.3 (99.4)
<i>I</i> / $\sigma$ ( <i>I</i> )	9.2 (2.0)	7.6 (1.6)	7.8 (1.6)	8.8 (1.6)	8.6 (1.7)	10.7 (2.2)
<i>R</i> <sub>merge</sub> (%) <sup>c</sup>	21.4 (131.2)	26.8 (159.4)	26.6 (156.5)	19.5 (159.0)	18.9 (153.7)	15.0 (116.3)
Data set	Native (A)	Native (B)	Native (C)	Ta SAD (A)		
Space group	P2 <sub>1</sub> 2 <sub>1</sub> 2 <sub>1</sub>	P2 <sub>1</sub> 2 <sub>1</sub> 2 <sub>1</sub>	I2 <sub>1</sub> 2 <sub>1</sub> 2 <sub>1</sub>	P2 <sub>1</sub> 2 <sub>1</sub> 2 <sub>1</sub>		
<i>Unit cell</i>						
<i>a</i> (Å)	132.1	149.7	161.0	130.4		
<i>b</i> (Å)	163.6	165.8	165.5	162.4		
<i>c</i> (Å)	536.9	537.8	536.2	536.5		
$\alpha$ (deg)	90	90	90	90		
$\beta$ (deg)	90	90	90	90		
$\gamma$ (deg)	90	90	90	90		
Wavelength (Å)	0.97926	0.97928	0.97928	1.25467		
Resolution (Å)	50–3.5 (3.61–3.50)	50–3.95 (4.16–3.95)	50–3.7 (3.92–3.70)	50–5.0		
Completeness (%)	99.9 (100.0)	99.4 (99.4)	99.4 (99.4)	99.3 (99.0)		
<i>I</i> / $\sigma$ ( <i>I</i> )	12.0 (1.9)	12.6 (1.9)	12.6 (1.9)	11.1 (3.5)		
<i>R</i> <sub>merge</sub> (%) <sup>c</sup>	16.1 (137.1)	14.1 (143.2)	10.4 (135.5)	13.8 (62.6)		
Number of reflections (total/unique)	1108 987/147 271	886 095/117 330	573 288/76 217			
Unique reflections (work/free)	145 735/1536	116 309/1021	75 374/843			
<i>R</i> <sub>work</sub> <sup>d</sup> / <i>R</i> <sub>free</sub> (%) <sup>e</sup>	29.7 (43.3)/ 33.5 (43.8)	35.0 (39.9)/ 37.3 (42.4)	31.8 (41.8)/ 33.3 (41.3)			
<i>RMSD</i>						
Bond (Å)	0.003	0.003	0.004			
Angle (deg)	0.648	0.643	0.722			
Ramachandran plot <sup>f</sup>	78.7/0.98	78.7/1.1	78.1/1.65			
Molecules/asymmetric unit	4	4	2			
Chain with $\alpha$ I domain	A	G				
Non-H atoms, protein/carbohydrate	49 614/570	49 515/673	23 978/404			
PDB code	3K6S	3K71	3K72			

<sup>a</sup>Numbers in parentheses correspond to the outermost resolution shell.<sup>b</sup>Letters in parentheses denote different crystal lattices.<sup>c</sup> $R_{\text{merge}} = \sum_i \sum_h |I_i(h) - \langle I(h) \rangle| / \sum_h \sum_i I_i(h)$ , where  $I_i(h)$  and  $\langle I(h) \rangle$  are the *i*th and mean measurement of the intensity of reflection *h*.<sup>d</sup> $R_{\text{work}} = \sum_h ||F_{\text{obs}}(h)| - |F_{\text{calc}}(h)|| / \sum_h |F_{\text{obs}}(h)|$ , where  $F_{\text{obs}}(h)$  and  $F_{\text{calc}}(h)$  are the observed and calculated structure factors, respectively. No *I*/ $\sigma$  cutoff was applied.<sup>e</sup> $R_{\text{free}}$  is the *R* value obtained for a test set of reflections consisting of a randomly selected ~1% subset of the data set excluded from refinement.<sup>f</sup>Residues in favourable and outlier regions of the Ramachandran plot as reported by MOLPROBITY (Davis *et al*, 2007).

(Table I). Multiple-wavelength Se anomalous diffraction (MAD) data sets in lattices A and C were collected to 3.8 and 4.0 Å, respectively. The initial Ta SAD phases were then combined with the Se MAD data set in lattice A to obtain experimental phases. These phases were extended by density modification to 3.5 Å native data for lattice A. The  $\alpha_X\beta_2$  structures built in lattice A were then used in molecular replacement to solve the structures in lattices B and C. The experimental phases for lattice C from Se MAD data were then obtained with help from the molecular replacement solution for lattice C and extended from 4.0 Å to native data

at 3.7 Å. We thus have experimental phases for lattices A and C at 3.5 and 3.7 Å, respectively, and a molecular replacement solution for lattice B at 3.95 Å.

The three lattices have unit cells with similar *b* and *c* dimensions. However, the *a* dimensions are about 132, 150, and 161 Å in lattices A, B, and C, respectively (Table I). All have 16  $\alpha_X\beta_2$  molecules per unit cell and either four or two molecules per asymmetric unit. The expansion along the *a* axis was accompanied by a change from P2<sub>1</sub>2<sub>1</sub>2<sub>1</sub> spacegroup in lattices A and B, which have four molecules per asymmetric unit, to I2<sub>1</sub>2<sub>1</sub>2<sub>1</sub> spacegroup in lattice C, which has two

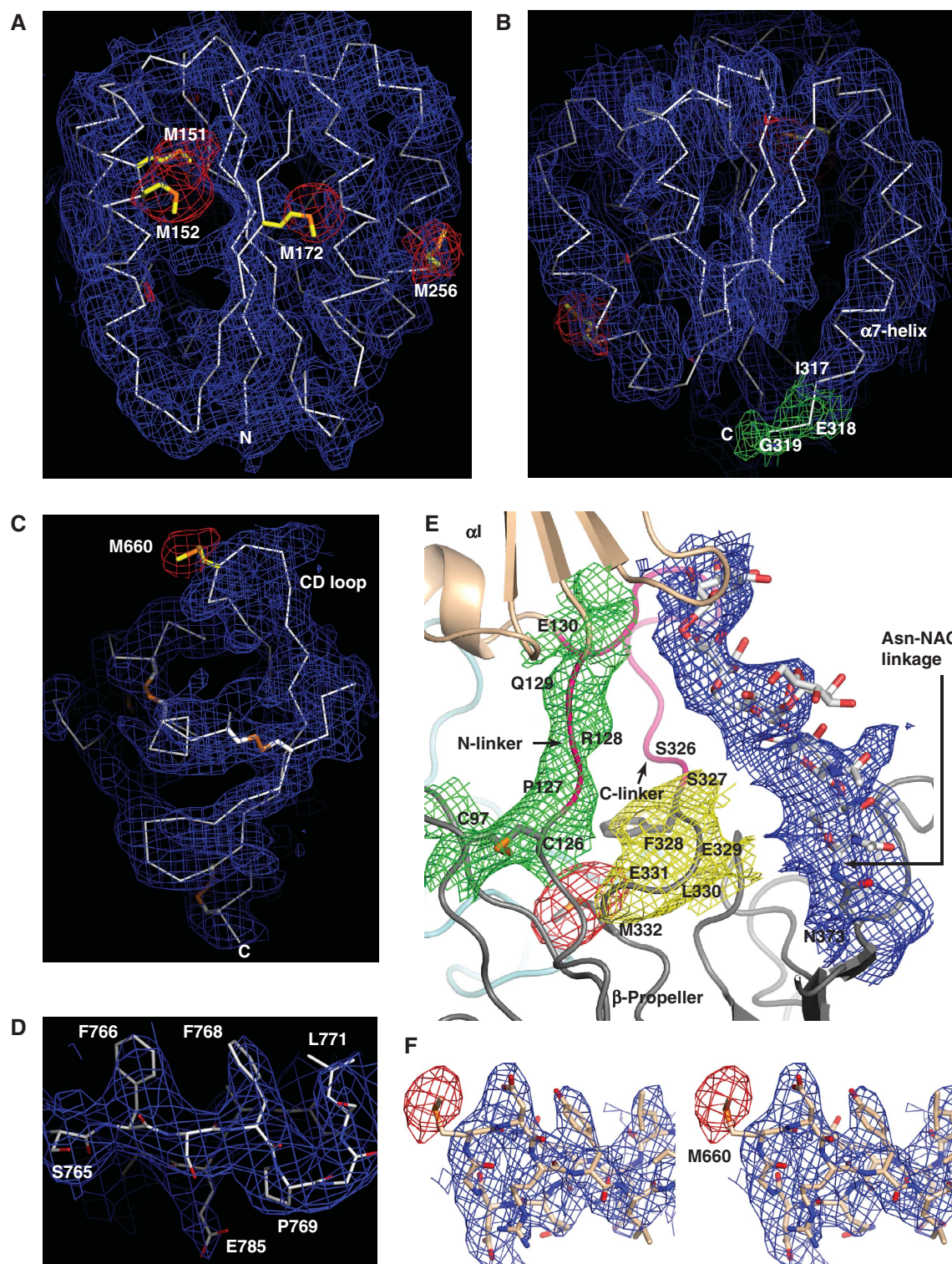


**Figure 1** Representative electron density. **(A, B)** The  $\alpha$ I domain. The main chain of  $\alpha$ I domain is shown in white. Se anomalous map is shown at 3  $\sigma$  level (red). Electron density map of  $\alpha$ I domain after multi-crystal averaging is at 1  $\sigma$  level (blue). Electron density around residues 318 and 319 is shown at 0.6  $\sigma$  in green. The methionine residues are shown in stick, with yellow carbon atoms and orange sulphur atoms. **(B)** Different view to show the electron density around the  $\alpha$ 7-helix. **(C, D)** Multi-crystal averaging electron density around  $\beta$ -tail domain **(C)** and around residues 765–771 and 783–786 in the calf-1 domain **(D)** Colours and map  $\sigma$  levels are as in **(A)**. **(E)** The  $\alpha$ I/ $\beta$ -propeller/ $\beta$ I domain interface. Multi-crystal averaging electron density map shown at 1  $\sigma$  level around  $\alpha$ -subunit  $\beta$ -propeller residue Asn-373 and its N-linked glycan (blue), the N-linker residues 127–130 and disulfide-bonded  $\beta$ -propeller residues C126 and C97 (green), and residues 326–327 of the C-linker and  $\beta$ -propeller residues 328–331 (yellow). The sidechains of residues C97, C126, F328, M332, N373 and its N-linked glycan are shown in stick. The electron density in this region shows distinct paths of the three segments, and clear connected density with the  $\beta$ -propeller domain. Se anomalous map is shown at 3  $\sigma$  level around the sidechain of Met-332.  $\alpha$  domain,  $\beta$ -propeller domain, and  $\beta$ I domain are in wheat, grey, and cyan, respectively. N- and C-linkers are in pink. The oxygen atoms, nitrogen atoms, and sulphur atoms are in red, blue, and orange, respectively. The carbon atoms of the glycan are in white. **(F)** Stereo image of  $\beta$ -tail domain CD loop. The oxygen, sulphur, nitrogen, and carbon atoms are in red, orange, blue, and wheat, respectively. Multi-crystal averaging map at 1  $\sigma$  is blue and Se anomalous map at 3  $\sigma$  level is red.



$\alpha_x\beta_2$  molecules per asymmetric unit (Table I). This expansion changed the packing environments around each molecule in the three lattices, so a total of 10 unique  $\alpha_x\beta_2$  molecules are defined.

Although our data are only at moderate to low resolution, the quality of the electron density maps has been greatly improved by multi-crystal averaging (Materials and methods). Typical density is shown for the  $\alpha$ I domain (Figure 1A and B) and  $\beta$ -tail domain (Figure 1C). At this resolution, small sidechains such as those of Ala, Ser, Val, and Thr may appear as bulges from the mainchain, but are not well resolved, whereas larger residues such as Leu, Met, Arg, Ile, Phe, Tyr, and Trp often show densities with identifiable, characteristic shapes (Figure 1D). Disulfide bonds were almost always seen as continuous density connected to the mainchain (Figure 1C and E). Individual atoms such as metals do not have separable density from coordinating sidechains; however, extra density and difference peaks may indicate their presence. The majority of the  $\alpha_x\beta_2$  mainchain has continuous density in the maps after multi-crystal averaging. The only exception is the  $\alpha$ I domain, which is disordered in some  $\alpha_x\beta_2$  molecules (see below). Tracing the mainchain was also aided by knowledge of domain folds from previous integrin structures. The only significant gap within an  $\alpha_x\beta_2$  molecule with an ordered  $\alpha$ I domain in the multi-crystal averaged maps was at the C-terminal connection between the  $\alpha$ I and  $\beta$ -propeller domains. At this location, the sequence to structure register was readily verified by density for Phe-328 and the anomalous signal for Met-332 (Figure 1E). Furthermore, density for the disulfide bond at the N-terminal connection between the  $\alpha$ I and  $\beta$ -propeller domains was readily apparent (Figure 1E). The mainchain trace and the sequence to structure register were validated with Se anomalous signals for the 25 Met residue positions. Density of average quality, over a stretch of residues with both small and large sidechains, is shown in Figure 1D.

### The $\alpha_x$ I domain

Of 10  $\alpha_x\beta_2$  molecules visualized in the three lattices, only two molecules show electron densities for  $\alpha$ I domains, in which lattice interactions stabilize their positions. The position of the  $\alpha$ I domain was clearly evident from electron density maps and from Se anomalous signals for the four Se-Met residues (Figure 1A and B). The  $\alpha_x$ I domain extends away from the remaining domains of CR4, which adopt a bent and compact conformation (Figure 2A). The  $\alpha$ I domain is inserted between blades 2 and 3 of the  $\alpha_x$   $\beta$ -propeller domain (Figure 3A and B; Supplementary Figure S1). The two linkers connecting the  $\alpha$ I and  $\beta$ -propeller domains are surprisingly flexible, and the  $\alpha$ I domain itself has no contact with the  $\beta$ -propeller and only a small contact with the specificity determining loop (SDL) of the  $\beta$ I domain (Figure 3B; Table II). Although not noted earlier (Nishida *et al*, 2006), EM also provided evidence for flexibility, with variation among class averages in orientation between the  $\alpha$ I domain and the  $\alpha_x\beta_2$  headpiece (Figure 2C–E; Supplementary Figure S2). Flexibility of the N-terminal (N) linker to the  $\alpha$ I domain is limited by its short length of three residues and an immediately preceding disulfide bond to a loop in  $\beta$ -propeller blade 2 (Figures 1E, 2A, 3A and B). However, the long, 10-residue Ser- and Thr-rich C-terminal (C) linker is highly flexible; even in the two ordered  $\alpha$ I domains, much of the C-linker shows

weak density. An N-linked oligosaccharide, among several protected from EndoH digestion, extends from the  $\beta$ -propeller to the  $\alpha$ I domain and partially shields the linkers (Figures 1E, 2A, 3A and B). Continuous densities to the  $\beta$ -propeller domain clearly distinguish the N-linker, C-linker, and N-glycan (Figure 1E). The linker regions of all  $\alpha$ I domains are flanked by N-glycosylation sites in the  $\beta$ -propeller, I domain, or linker itself; glycans here may circumscribe flexibility and shield the flexible C-linker from proteolysis.

$\alpha$ I and  $\beta$ I domains have structurally homologous  $\alpha/\beta$  folds, with a metal ion-dependent adhesion site (MIDAS) that binds a  $Mg^{2+}$  ion (Springer and Wang, 2004; Luo *et al*, 2007). Density suggests the presence of a metal ion at the  $\alpha_x$  MIDAS. Three different conformations termed closed, intermediate, and open have been defined for  $\alpha$ I domains (Springer and Wang, 2004; Luo *et al*, 2007). The positions of the  $Mg^{2+}$ , the Asp-X-Ser-X-Ser MIDAS motif, and the C-terminal  $\alpha$ 7-helix (Figure 1E) show that the  $\alpha_x$ I domain is in the closed, low-affinity conformation similar to that of the isolated  $\alpha_x$ I domain (Supplementary Figure S4) (Vorup-Jensen *et al*, 2003).

### The $\beta_2$ I domain

In  $\beta_3$  integrins, the  $\beta_3$ I domain has been shown to have two conformations, termed closed and open (Luo *et al*, 2007). The  $Mg^{2+}$ -binding  $\beta$ I domain MIDAS is flanked on either side by  $Ca^{2+}$ -binding adjacent to MIDAS (ADMIDAS) and synergistic metal-binding sites (SYMBs) (Xiong *et al*, 2001, 2002; Xiao *et al*, 2004; Zhu *et al*, 2008). In the bent  $\alpha_x\beta_2$  structure, the  $\beta_2$ I domain is in a low-affinity, closed conformation similar to that seen in  $\beta_3$  integrins, as shown by the positions of the  $\beta_2$ I domain Asp-X-Ser-X-Ser motif and C-terminal  $\alpha$ 7-helix, and the swung-in hybrid domain (Figure 3C, F and G). Electron density suggests that metal ions occupy the  $\beta$ I ADMIDAS, and possibly the SYMBs, but not the MIDAS. Lack of metal ions at the SYMBs and ADMIDAS may in part be due to use of the crystallization precipitants citrate and phosphate, which compete for metal ions.

In a surprising contrast to previous integrin  $\beta_3$  and  $\alpha$ I domain structures, an extra acidic residue is found at the  $\beta_2$  MIDAS, Asp243 (Figure 3F). Although density for a metal ion is absent, the position of the Asp243 sidechain suggests that it could directly coordinate  $Mg^{2+}$ . This has important implications, because direct coordination of this Asp with  $Mg^{2+}$  would reduce its electrophilicity, and hence decrease affinity for its intrinsic ligand (see below).

The  $\beta_2$ I domain also shows an extra acidic residue at the ADMIDAS, Glu-325 (Figure 3F). The backbone carbonyl oxygen of Glu-325 coordinates the ADMIDAS  $Ca^{2+}$  ion similarly to Met-335 in  $\beta_3$ . Although the Glu-325 sidechain is only partially in density, it has the potential to coordinate the ADMIDAS in the closed conformation (Figure 3F) or during transition to the high-affinity, open conformation.

### Overall bent conformation and differences from $\alpha$ I-less integrins

Apart from the  $\alpha$ I domain, the 12 other domains in  $\alpha_x\beta_2$  have excellent density in all 10 molecules, including the two domains at the  $\beta$ -knee, I-EGF domains 1 and 2. These 12 domains assume a bent conformation as found in the  $\alpha$ I-less integrins  $\alpha_v\beta_3$  (Xiong *et al*, 2001, 2002) and  $\alpha_{IIb}\beta_3$  (Zhu *et al*, 2008) (Figure 2A and G). The leg domains tuck tightly

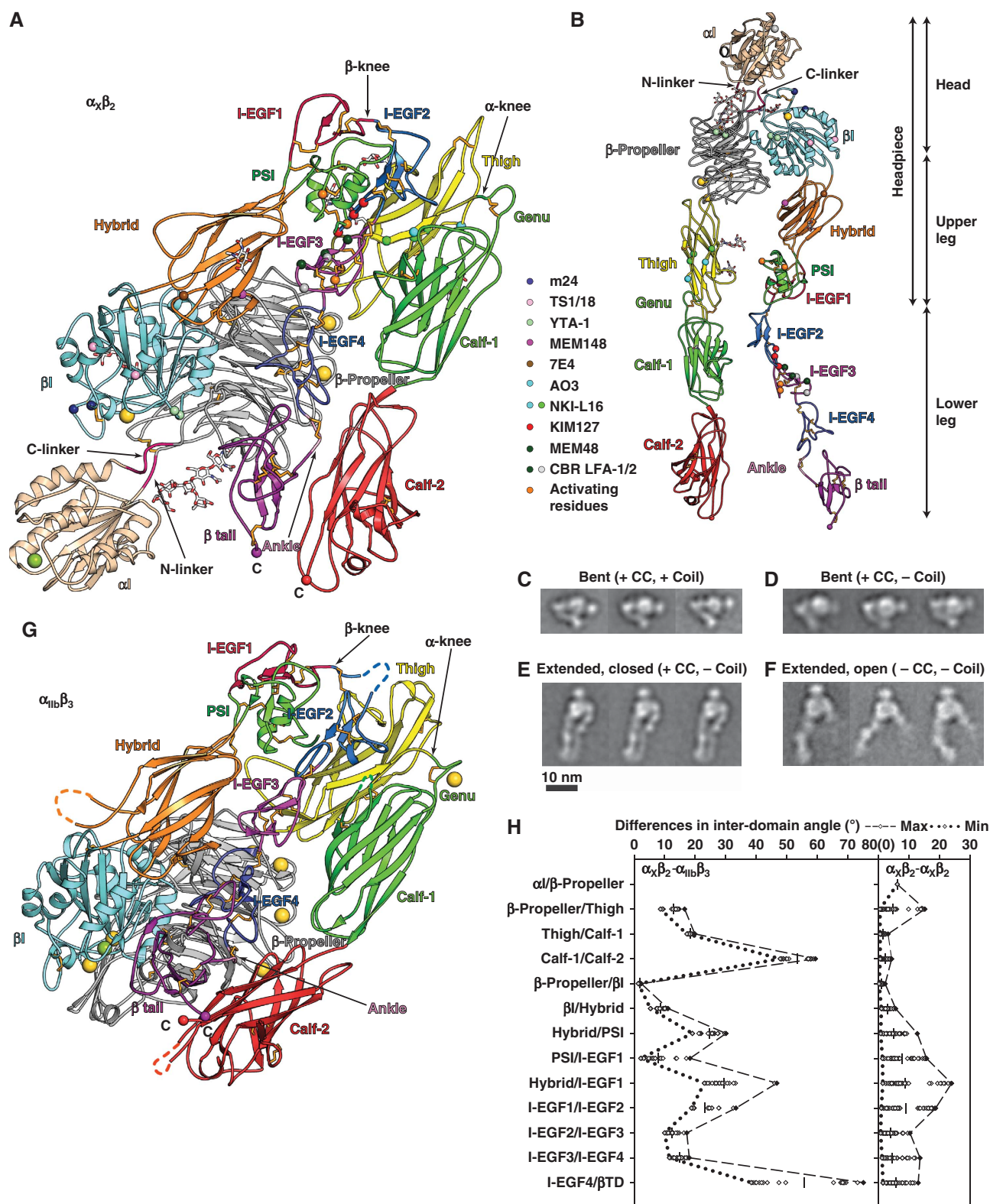


**Figure 2** Structure of CR4, integrin  $\alpha_x \beta_2$ . (A) Cartoon of  $\alpha_x \beta_2$  molecule 1 in lattice A and (B) an extended model made by adjusting domain interfaces at and near the knees. Disulfides are gold sticks, and glycans are sticks with white carbons. Ca and Mg ions are gold and green spheres, respectively. Smaller spheres show C $\alpha$  atoms of conformation-associated epitopes and C-terminal residues. (C–F) Representative  $\alpha_x \beta_2$  EM class averages. The presence (+) or absence (–) of a disulfide after the  $\alpha_x$  and  $\beta_2$  C-termini (CC) and subsequent linker and coiled-coil (coil) is indicated. (G) Cartoon of  $\alpha_{11b} \beta_3$  (Zhu *et al*, 2008) in same orientation and style as  $\alpha_x \beta_2$  in (A). (H) Differences in interdomain angles between 10 molecules of  $\alpha_x \beta_2$  and 2 molecules of  $\alpha_{11b} \beta_3$  (left panel), or among 10 molecules of  $\alpha_x \beta_2$  (right panel). The mean values of interdomain angles are shown as bars and the maximal and minimal angles are shown in dashed or dotted lines, respectively.

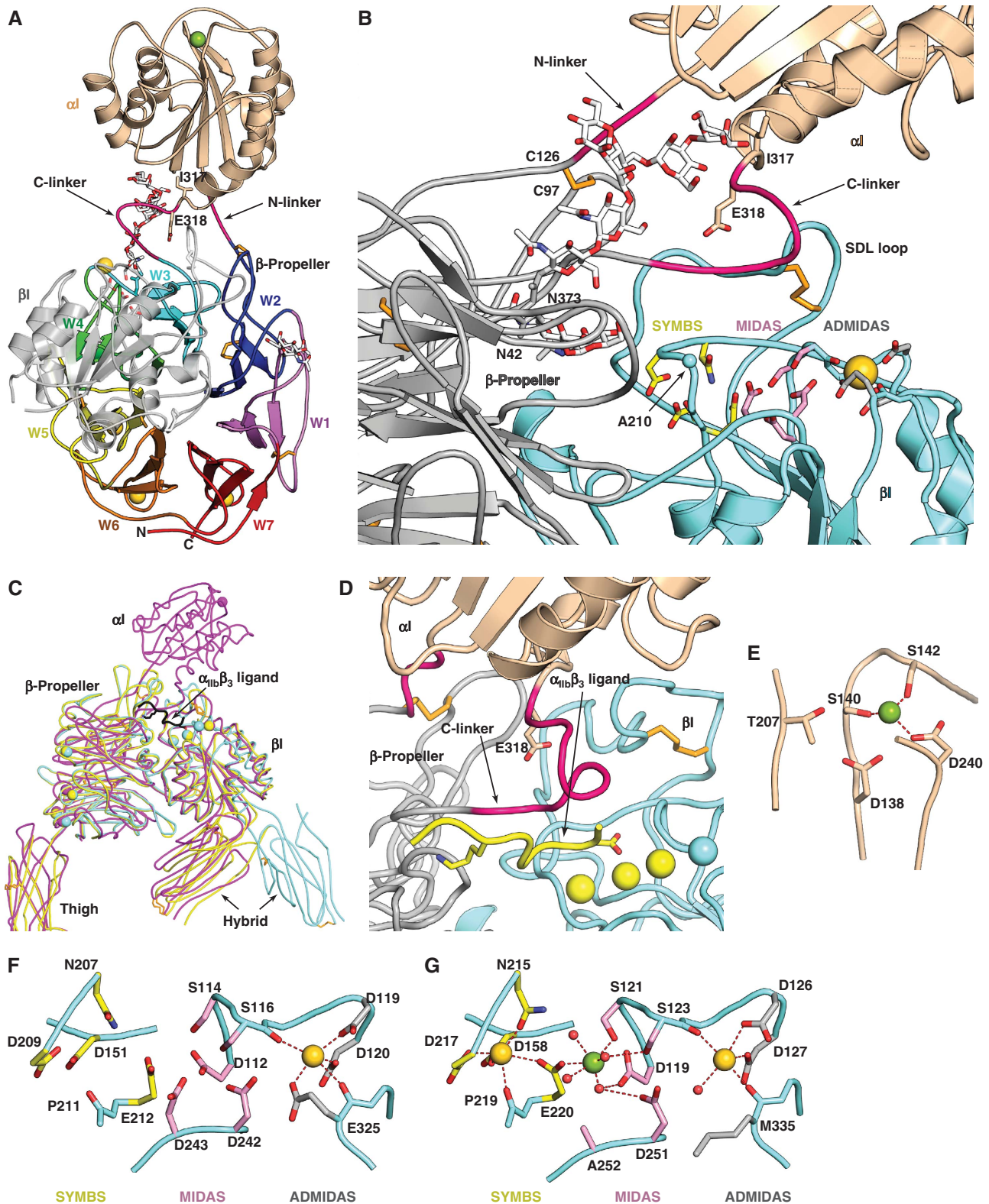


**Figure 3** The  $\alpha$ l,  $\beta$ l, and  $\beta$ -propeller domain interface, and I domain metal-binding sites. (A, B) The interface. Representations are as in Figure 2A and B; additionally, the indicated sidechains and backbone carbonyls are shown as sticks. (C) Superposition of headpieces from  $\alpha_x\beta_2$  (magenta), unliganded-closed  $\alpha_{ib}\beta_3$  (Zhu *et al*, 2008) (yellow) and liganded-open (Springer *et al*, 2008)  $\alpha_{ib}\beta_3$  (cyan, with ligand in black). (D) Enlarged view of the superposition in (C) showing only  $\alpha_x\beta_2$  (with its ADMIDAS metal as cyan sphere) and the ligand and SYMBs, MIDAS, and ADMIDAS metals from liganded-open  $\alpha_{ib}\beta_3$  (yellow). (E–G) Metal coordination sites, with coordinations dashed. (E)  $\alpha$ l domain MIDAS. (F, G)  $\beta$ l domain metal-binding sites in  $\alpha_x\beta_2$  (F) and unliganded-closed  $\alpha_{ib}\beta_3$  (G).

against one another, and against the headpiece, owing to sharp bends at the  $\alpha$ - and  $\beta$ -knees. As  $\alpha$ l and  $\alpha$ l-less integrins are among the most distantly related members of the

integrin family, the bent conformation appears to be a general characteristic of the low-affinity integrin state (Nishida *et al*, 2006).



**Table II** Solvent accessible surfaces buried in bent  $\alpha_x\beta_2$ <sup>a</sup>

	Headpiece–tailpiece		$\alpha$ Headpiece– $\beta$ headpiece; $\alpha$ tailpiece– $\beta$ tailpiece		Domain junctions <sup>b</sup>	
Domain	Solvent accessible surface area buried (Å <sup>2</sup> )					
	$\alpha_x\beta_2$	$\alpha_{Iib}\beta_3$	$\alpha_x\beta_2$	$\alpha_{Iib}\beta_3$		$\alpha_x\beta_2$ $\alpha_{Iib}\beta_3$
$\alpha$ I	0	—	188	—	$\alpha$ I—N- and C-linkers	475 —
N- and C-linkers	0	—	34	—	N- and C-linkers– $\alpha\beta$ -propeller	451 —
$\alpha\beta$ -propeller	639	235	1606	1854	$\alpha\beta$ -propeller– $\alpha$ -thigh	1054 833
$\alpha$ -thigh	383	314	0	0	$\alpha$ -thigh– $\alpha$ calf-1	880 914
$\alpha$ calf-1	19	113	609	367	$\alpha$ calf-1– $\alpha$ calf-2	726 770
$\alpha$ calf-2	241	0	406	636	$\beta$ PSI– $\beta$ hybrid	781 759
$\beta$ PSI	366	151	0	0	$\beta$ PSI– $\beta$ I-EGF1	1048 848
$\beta$ I	28	1	1752	1766	$\beta$ hybrid– $\beta$ I	1412 1610
$\beta$ hybrid	91	671	16	172	$\beta$ hybrid– $\beta$ I-EGF1	0 20
$\beta$ I-EGF1	0	0	0	0	$\beta$ I-EGF1– $\beta$ I-EGF2	564 463
$\beta$ I-EGF2	662	395	303	188	$\beta$ I-EGF2– $\beta$ I-EGF3	574 550
$\beta$ I-EGF3	313	460	320	153	$\beta$ I-EGF3– $\beta$ I-EGF4	541 402
$\beta$ I-EGF4 <sup>b</sup>	300	358	171	338	$\beta$ I-EGF4– $\beta$ -tail	744 435
$\beta$ -tail	51	56	239	312		
Total	3093	2754	5644	5786		9250 6840

<sup>a</sup>Calculated with AREAIMOL of CCP4 using chains A and B of lattice A for  $\alpha_x\beta_2$  and chains A and B of  $\alpha_{Iib}\beta_3$  (Zhu *et al*, 2008).

<sup>b</sup>Including  $\beta$ -ankle.

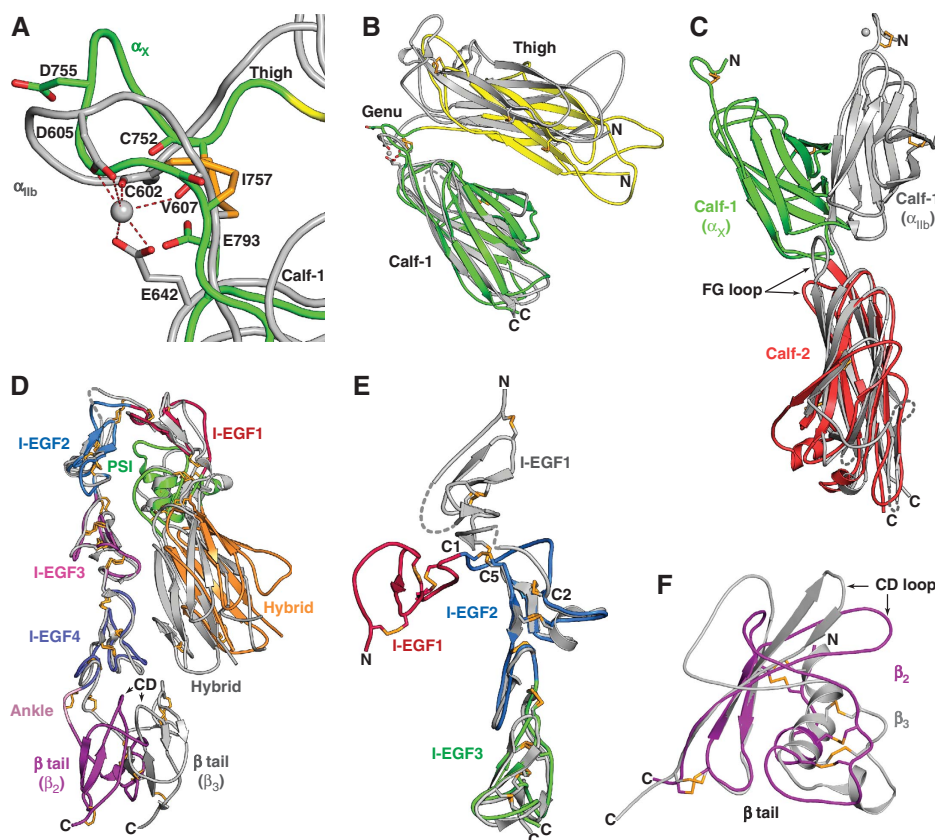


**Figure 4** Integrin leg domains. Domains in  $\alpha_x\beta_2$  are coloured as in Figure 2A and B and in other integrins are silver with dashes for disordered loops and metals as spheres. (A) The genu. (B) The  $\alpha_x$  and  $\alpha_{Iib}$  thigh and calf-1 domains superimposed on calf-1. (C) The  $\alpha_x$  and  $\alpha_{Iib}$  calf-1 and calf-2 domains superimposed on calf-2. (D) The  $\beta_2$  and  $\beta_3$  (Zhu *et al*, 2008) legs superimposed on I-EGF domains 2–4. (E) Bent intact  $\beta_2$ -leg and  $\beta_3$ -leg fragment (Shi *et al*, 2007) superimposed on I-EGF2. (F) Superimposed  $\beta_2$  and  $\beta_3$  (Xiong *et al*, 2001)-tail domains.

However, there are important differences in packing interactions and orientations. Compared to  $\alpha_v$  and  $\alpha_{Iib}$ , the  $\alpha_x$  genu has a different backbone conformation (Figure 4A). The metal-coordinating residues are conserved in the  $\alpha_x$  genu (Supplementary Figure S5a), but because of the different backbone conformation, their geometry is not appropriate

for binding a  $\text{Ca}^{2+}$  ion. This surprising finding shows the conformational plasticity of this disulfide-bonded, 7-residue loop. Furthermore, the thigh and calf-1 domains approach more closely in  $\alpha_x\beta_2$  than in  $\alpha_v\beta_3$  or  $\alpha_{Iib}\beta_3$  (Figure 4B). Moreover, the orientation between the calf-1 and calf-2 domains differs by 50° between  $\alpha_x\beta_2$  and  $\beta_3$  integrins

(Figures 2A, G, H and 4C; Supplementary Figure S4a–c), with the FG loop of calf-2 squashed by the calf-1 domain in  $\alpha_X$  (Figure 4C). This results in a wider cleft between the upper  $\beta$ -leg and lower  $\alpha$ -leg in  $\alpha_X\beta_2$  than in  $\alpha_{IIB}\beta_3$ ; that is, a greater separation between the  $\beta$ I and calf-2 domains (Figure 2A and G). The lower  $\beta$ -leg is tucked in a cleft, between the upper  $\beta$ -leg on one side and the  $\alpha$ -subunit on the other. Thus, this cleft is wider, particularly at its base near the membrane, in  $\alpha_X\beta_2$  than in  $\alpha_{IIB}\beta_3$ . The base of  $\alpha_X$  calf-2 has several loops that differ markedly from those in  $\alpha_V$  and  $\alpha_{IIB}$  (Figure 4C), and includes a membrane-proximal  $\alpha$ -helix in the XY loop that is cleaved by furin in most  $\alpha$ I-less integrins but not  $\alpha$ I integrins (Figure 4C; Supplementary Figure S1).

The orientation between the I-EGF4 and  $\beta$ -tail domain differs by 40–70° between  $\alpha_X\beta_2$  and  $\alpha_{IIB}\beta_3$  (Figures 2H and 4D); indeed, the orientations at the last interdomain interfaces in both the  $\alpha$ - and  $\beta$ -subunits show the greatest differences between  $\alpha_X\beta_2$  and  $\alpha_{IIB}\beta_3$  (Figure 2H), a specialization that may accommodate the  $\alpha$ I domain. The base of the calf-2 domain is broad and may help together with the  $\beta$ -tail domain to orient bent integrins on the cell surface. Assuming that the calf-2 domains of  $\alpha_X\beta_2$  and  $\beta_3$  integrins would be approximately normal to the membrane, the overall effect of the different orientations at the calf-1/calf-2 and I-EGF4/ $\beta$ -tail interfaces is to provide clearance between the  $\alpha$ I domain and the plasma membrane in  $\alpha$ I integrins (Figure 2A and G; Supplementary Figure S4). However, flexibility of the linkers between the ectodomain and the transmembrane domains may enable substantial rigid body movement of the ectodomain relative to the membrane, as has been found for  $\alpha_{IIB}\beta_3$  (Zhu *et al*, 2009).

### The ectodomain-transmembrane domain linkers

A disulfide bond in the construct used for crystallization was designed to mimic the clasp between associating transmembrane domains. Cysteines are present at the ends of the linkers following the  $\alpha_X$  calf-2 and  $\beta_2$   $\beta$ -tail domains, immediately preceding the position of transmembrane domains in the native protein. Complete sets of negative stain EM class averages for  $\alpha_X\beta_2$  molecules with four different types of C-terminal clasps are compared in Supplementary Figure S2. Constructs containing a C-terminal coiled-coil are the most constrained, with all particles in the bent conformation, whether or not a C-terminal disulfide is present (Figure 2C; Supplementary Figure S2c) or absent (Supplementary Figure S2d). When a C-terminal disulfide is present, and the coiled-coil is removed, as in the construct that was crystallized, particles that are bent (Figure 2D), and are extended with a closed headpiece (Figure 2E), are both present (Supplementary Figure S2e). Furthermore, this preparation, as similarly shown for a preparation with a coiled-coil (Nishida *et al*, 2006), adopts the extended, open headpiece conformation in presence of CBR-LFA-1/2 and KIM127 Fab (data not shown). Therefore, the C-terminal disulfide used in these studies does not constrain a particular integrin conformation. When neither a C-terminal disulfide nor a coiled-coil is present, particles that are bent, extended with the closed headpiece or extended with the open headpiece, are all present (Figure 2F; Supplementary Figure S2f).

Among 10  $\alpha_X\beta_2$  molecules in our crystal structures, the orientation between the calf-2 and  $\beta$ -tail domains differs (Supplementary Figure S3a), and thus is not constrained by

the C-terminal disulfide bond. Furthermore, the ectodomain-transmembrane domain linkers are flexible. The last residue of the calf-2 domain is Tyr-1081, and the only linker residue seen in density is Lys-1082. Four further linker residues precede the TM domain in the native  $\alpha_X$ -subunit, Val-His-Asn-Pro (Supplementary Figure S1a). The corresponding Val-His-Gly-Cys sequence in the clasped construct is disordered. The last residue of the  $\beta$ -tail domain is Cys-673. Among the 10  $\alpha_X\beta_2$  molecules, the last residue seen in density is either Cys-673 or linker residue Val-674. Four further linker residues precede the TM domain in the native  $\beta_2$ -subunit, Ala-Gly-Pro-Asn. The corresponding Ala-Gly-Pro-Asp-Gly-Cys sequence in the clasped construct is disordered. Among the 10  $\alpha_X\beta_2$  molecules, the distance between the last calf-2 and  $\beta$ -tail domain residues is 14–16 Å. A vast number of backbone conformations would be available for the five linker residues in each subunit to span this distance and join together either in a disulfide bond in the crystallized construct or at the beginning of two associated transmembrane  $\alpha$ -helices in the native protein.

The disorder observed in the ectodomain-transmembrane domain linkers in our structure is entirely consistent with the lack of ordered structure of the same region in recently published NMR and Disulfide/Rosetta structures of the membrane-embedded region of integrin  $\alpha_{IIB}\beta_3$  (Lau *et al*, 2009; Zhu *et al*, 2009). Among the four  $\alpha$ -subunits that associate with the  $\beta_2$ -subunit, neither the sequence nor the length of the linker is conserved (Supplementary Figure S6b). All this evidence strongly suggests that the linkers between the ectodomain and TM domain are flexible, and hence do not constrain the orientation between the ectodomain and the membrane. This conclusion is consistent with previous evidence from disulfide crosslinking within the linker region of  $\alpha_{IIB}\beta_3$ , and building models consistent with the restraints, which showed that flexion of the ectodomain was limited only by the steric barrier of the lipid bilayer (Zhu *et al*, 2009). As pointed out earlier, this also has important implications for transmembrane signalling, because large movements

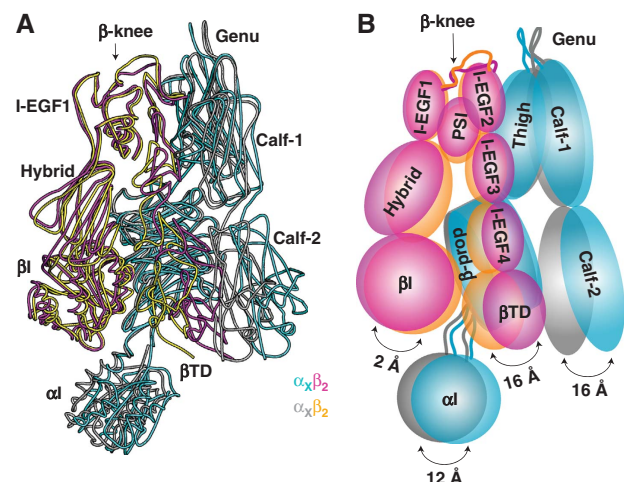


**Figure 5** Breathing of bent  $\alpha_X\beta_2$ . (A) Two representative diverse structures after superposition of all 10 molecules on all domains except  $\alpha$ I (shown are chains G and H of lattice A with the  $\alpha$ I domain from chain A and chains C and D of lattice A with the  $\alpha$ I domain from chain G of lattice B). (B) Schematic showing maximal differences in position after superposition.



such as transmembrane domain separation, but not small movements such as transmembrane domain pivoting or pistoning, could be transmitted through the flexible linkers (Zhu *et al*, 2009).

### Ectodomain flexibility

The 10 examples of  $\alpha_X\beta_2$  visualized in three different crystal lattices (Table I) provide unprecedented information on integrin flexibility (Figures 2H and 5). Overall, more variation in interdomain angle occurs between the small domains in  $\beta_2$  than between the robust domains in  $\alpha_X$  (Figure 2H). Within  $\beta_2$  the greatest interdomain variation is seen at hybrid/I-EGF1 and I-EGF1/I-EGF2 interfaces at the  $\beta$ -knee. Surprisingly, in  $\alpha_X$  the greatest flexibility is found at the  $\beta$ -propeller/thigh interface, rather than at the thigh/calf-1 interface at the  $\alpha$ -knee (Figure 2H). This finding is consistent with the long, open loops in the thigh domain that flank the  $\beta$ -propeller domain in  $\alpha_X$  (Figures 2B and 3C).

The overall effect of flexibility at multiple domain interfaces results in variation in up to 16 Å in the position of domains that are membrane-proximal in the bent conformation (Figure 5A and B). This breathing substantially opens the cleft bearing the lower  $\beta$ -leg, between the upper  $\beta$ -leg and lower  $\alpha$ -leg. The lower  $\beta$ -leg moves largely in sympathy with the lower  $\alpha$ -leg, away from the upper  $\beta$ -leg (Figure 5A). Cleft opening enables egress of the lower  $\beta$ -leg before integrin extension.

### The $\beta_2$ -knee and $\alpha_X\beta_2$ extension

In integrin extension, by far the largest changes in interdomain orientation occur at the  $\alpha$ - and  $\beta$ - knees, which transition from highly bent to extended conformations (Figure 2C–F). In the  $\beta_2$ -leg, there is an acute bend between I-EGF domains 1 and 2, whereas there is a distinctive, extended conformation at the junctions between I-EGF domains 2 and 3 and between domains 3 and 4 (Figures 2A and 4D).

Integrin EGF domains are a distinctive subfamily of EGF domains, with an additional disulfide bridge between cysteines 1 (C1) and 5 (C5) in each domain (Takagi *et al*, 2001; Beglova *et al*, 2002; Zhu *et al*, 2008). Only a single residue intervenes between C8 of one domain and C1 of the next domain, at a Cys-X-Cys junction. It has been suggested earlier that the extra C1–C5 disulfide in I-EGF domains is a specialization that enables moderate, but not extreme, motion at the interdomain junctions, and that the amount of motion that can occur is modulated by the length of the C1–C2 loop. The interdomain junction is referred to as gimbal-like, because there are two types of motion, one in the Cys-X-Cys backbone, and a second in the C1–C2 loop, involving both the C1–C2 backbone, and rotameric changes of the C1 sidechain (Zhu *et al*, 2008).

$\beta_2$ -leg fragment crystal structures (Shi *et al*, 2007) that extend either through I-EGF2 or I-EGF3 provide two examples of the I-EGF domain 1/domain 2 interface and one example of the I-EGF domain 2/domain 3 interface for comparison to the interfaces in the bent conformation. The bend between I-EGF domains 1 and 2 in the bent conformation is far more acute than seen in either of the two examples of  $\beta_2$ -leg fragments, which by comparison are more extended in conformation (Shi *et al*, 2007; Zhu *et al*, 2008) (Figure 4E). More movement at the gimbal-like  $\beta$ -knee occurs by flexion of the tip of I-EGF2 within its first disulfide-bonded C1–C2 loop than at the Cys-

X-Cys junction with I-EGF1 (Figure 4E). Thus, the backbone conformation of the 13 residues between C1 and C2 of I-EGF2 varies greatly between the bent and extended conformations, and a portion of this loop is disordered in the more extended, and higher resolution,  $\beta_2$ -leg fragment (Figure 4E). As emphasized earlier, the C1–C2 loop is much longer in I-EGF2 than in other I-EGF domains, enabling substantial flexibility important for integrin extension (Zhu *et al*, 2008). The flexibility of this loop is further emphasized by the presence of different I-EGF2 C1–C2 loop conformations in different examples of bent  $\alpha_X\beta_2$  molecules (Figure 5A), and by missing density in this loop in a bent integrin  $\alpha_{IIb}\beta_3$  crystal structure (Zhu *et al*, 2008).

Among I-EGF domains, I-EGF3 has the shortest C1–C2 loop, with four residues between C1 and C2. Remarkably, the orientation between I-EGF domains 2 and 3 is essentially identical in crystals of bent  $\alpha_X\beta_2$  and the  $\beta_2$ -leg fragment (Figure 4E). This suggests that this interface is relatively rigid, and that the extended conformation at this interface would also be seen in extended  $\alpha_X\beta_2$ . Furthermore, the results support the suggestion that the length of the loop between C1 and C2 of I-EGF domains correlates with interdomain flexibility (Zhu *et al*, 2008).

### Structural evidence that destabilizing the bent conformation favours integrin activation

$\alpha_X\beta_2$  containing a human  $\alpha_X$ -subunit and chicken  $\beta_2$ -subunit is constitutively active in binding iC3b. The minimal substitutions for activation of CR4 activity were found to be  $\beta_2$  Q525S and V526L, and it was suggested earlier that these mutations were in an interface with  $\alpha_X$  that stabilized CR4 in the resting state (Zang and Springer, 2001). Indeed, as predicted, the structure shows that these residues locate to a loop of I-EGF3 in the lower  $\beta_2$ -leg that is deeply buried in the bent conformation in a crevice between the  $\alpha_X$  thigh and calf-1 domains (Figure 2A), but is exposed in the extended conformation (Figure 2B). Thus, these substitutions appear to destabilize the bent conformation, and induce CR4 activation by favouring the extended conformation.

KIM-127 is an antibody that reports integrin activation; CBR-LFA-1/2 is an antibody that induces activation. Their epitopes have been mapped earlier to individual mouse/human amino acid substitutions (Lu *et al*, 2001a). The KIM-127 epitope is buried on I-EGF2, in an interface with the PSI domain (Figure 2A and B). The CBR-LFA-1/2 epitope is buried on I-EGF3 in an interface with the hybrid domain (Figure 2A and B). Both epitopes would be exposed on integrin extension.

The AO3 and NKI-L16 Abs to  $\alpha_L$  induce or report activation of integrin  $\alpha_L\beta_2$ , and have also been mapped to individual human/mouse substitutions (Xie *et al*, 2004). Mapping these residues onto  $\alpha_X$  shows that these Abs bind to the face of the thigh domain that is buried by calf-1 in the bent conformation, but would be exposed after extension (Figure 2A and B).

These results show a close association of the inactive  $\beta_2$  integrin state with the bent conformation, and close association of the active  $\beta_2$  integrin state with the extended conformation. The results are in excellent agreement with EM studies on complexes between Fab and integrin  $\alpha_X\beta_2$  that have shown that KIM-127 Fab that reports  $\beta_2$  integrin activation on cell surfaces binds only to the extended conformation, and that CBR-LFA-1/2 Fab that activates  $\beta_2$  integrins on cell surfaces induces extension (Nishida *et al*, 2006). Together

with the earlier EM studies, and functional experiments with these antibodies on intact cells, this work definitively establishes that integrin extension is sufficient to induce activation and occurs during physiologic integrin activation.

### **Antibodies that discriminate between the closed and open headpiece conformations**

The effects of further activating antibodies cannot be explained solely by inducing integrin extension, because they either bind to epitopes that are completely exposed in the bent conformation, or bind to regions that move in allostery. Furthermore, some inhibitory antibodies do not act by blocking ligand binding, because they do not bind to the  $\alpha_X$ I domain. The locations of all of these epitopes map to regions of the  $\beta$ I and hybrid domains that shift in allostery, and they support the importance of conversion from the closed to open headpiece conformation in  $\beta_2$  integrin activation.

Some of these antibodies bind to epitopes that are fully exposed in the bent conformation. The activation-dependent m24 epitope maps to residues that are exposed in both the bent and extended conformations in the  $\beta$ I SDL and  $\alpha$ 1-helix (Lu *et al*, 2001b; Kamata *et al*, 2002) (Figure 2A and B);  $\alpha$ 1-helix movement alters the relative disposition of these residues in the open headpiece (Xiao *et al*, 2004). Conversely, the allosterically inhibitory TS1/18 Ab binds to  $\beta$ I residues on the  $\alpha$ 1- and  $\alpha$ 7-helices that are exposed in both the bent and extended conformations (Figure 2A and B) (Lu *et al*, 2001b); these residues would be further apart on helix movement in the open headpiece conformation (Xiao *et al*, 2004). The inhibitory 7E4 Ab binds to an outer hybrid/ $\beta$ I domain interface that is well exposed in the bent and extended, closed headpiece conformations (Figure 2A and B); this Ab is predicted to stabilize the closed headpiece conformation (Tng *et al*, 2004).

Other antibodies, all of which are activating, bind to epitopes that are masked in the bent conformation, but may (YTA-1) or must (MEM148) also favour the open headpiece conformation. The activation-associated YTA-1 epitope maps to residues in the  $\beta$ 5- $\alpha$ 6 loop of the  $\beta$ I domain that are shielded by the  $\beta$ -tail domain in the bent, closed headpiece conformation (Figure 2A) and might also change conformation in the open headpiece (Zang *et al*, 2000). The activation-reporting MEM148 Ab binds to an inner hybrid/ $\beta$ I domain interface (Tang *et al*, 2005) that is masked in the bent/closed and extended/closed conformations by the  $\beta$ -propeller domain (Figure 2A and B); headpiece opening is required for epitope exposure. Together, the localization of the epitopes for antibodies that allosterically activate or inhibit  $\beta_2$  integrin function shows that not only extension but also headpiece opening is required for  $\beta_2$  integrin activation.

### **Disulfide bond exchange in integrins is not supported**

On the basis of the presence of a CGXC sequence in each of four cysteine-rich repeats in integrins, a motif that is also found at the active site of thioredoxin, a thiol-isomerase activity has been hypothesized and found in integrin  $\alpha_{IIb}\beta_3$  (O'Neill *et al*, 2000). In thiol and disulfide isomerases, the two cysteines of the CGXC motif are alternatively disulfide bonded to one another, or reduced. However, I-EGF domains have a fold quite distinct from that in these isomerases, and the two cysteines in the CGXC motif are not bonded to one another, but correspond to C5 and C6, which are present in

the C1-C5 and C3-C6 disulfides. Multiple reduced cysteines have been reported to be present in the cysteine-rich repeats of  $\alpha_{IIb}\beta_3$  isolated from outdated platelets (Yan and Smith, 2001). However, other studies have found no significant number of reactive cysteines on transfectants (Luo *et al*, 2004). A classic study, on fresh platelets, found that though a single reduced cysteine in the cytoplasmic domain of platelet GPIIb $\beta$  (25 000 molecules/cell) was readily detected, none were present in the integrin  $\alpha_{IIb}$  or  $\beta_3$ -subunits (100 000 molecules/cell) (Kalomiris and Collier, 1985). In agreement, the crystal structure of the integrin  $\alpha_{IIb}\beta_3$  ectodomain shows that all cysteines are paired (Zhu *et al*, 2008). In the multi-crystal averaged density for the  $\alpha_X\beta_2$  structures reported here, density for disulfide bonds is in general well defined and easily traced (Figure 1C and E). All cysteines, except Cys-444 that is buried in the  $\beta$ -propeller domain, are present in disulfide bonds. Likewise, all cysteines present in three different high-resolution structures of  $\beta_2$  integrin leg fragments are disulfide bonded (Shi *et al*, 2005, 2007). Thus, as described above, extension at the  $\beta$ -knee, with large leg rearrangements at the I-EGF1/I-EGF2 interface, can occur without reduction (Figure 2C-F). It should be noted that substantial rearrangement of the C1-C5 disulfide bond, with change in the C1 cysteine rotamer, can occur without reduction, because of the backbone flexibility afforded by the long C1-C2 loop in I-EGF2.

### **Structural refutation of the deadbolt model**

On the basis of the  $\alpha_V\beta_3$  structure, a CD loop 'deadbolt' in the  $\beta$ -tail domain has been proposed to contact the  $\beta$ I domain and restrain it in the closed conformation (Xiong *et al*, 2003). However, the interface of 40 Å<sup>2</sup> (Xiong *et al*, 2001) or 10 Å<sup>2</sup> (Xiong *et al*, 2009) is so small that it would be surprising if it were significant (Lo Conte *et al*, 1999). Deletion and mutation of the CD loop in integrins  $\alpha_V\beta_3$  and  $\alpha_{IIb}\beta_3$  have been shown to have no effect on their activation (Zhu *et al*, 2007). Furthermore, a lack of any interface between the  $\beta$ -tail CD loop and the  $\beta$ I domain was found in an  $\alpha_{IIb}\beta_3$  crystal structure (Zhu *et al*, 2008). Thus, the deadbolt hypothesis has been disproved in integrins with the  $\beta_3$ -subunit, on which this hypothesis was based.

The only mutational test of the deadbolt hypothesis interpreted in its support is a study with the integrin  $\beta_2$ -subunit, in which  $\beta$ -tail CD loop substitution and deletion were found to activate integrin  $\alpha_M\beta_2$  (Gupta *et al*, 2007). However,  $\alpha_X\beta_2$  and  $\alpha_V\beta_3$  differ markedly in the conformation of the  $\beta$ -tail domain, including the CD loop (Figure 4F). Furthermore, the orientation of the  $\beta$ -tail domain within the  $\beta$ -leg differs markedly between  $\alpha_X\beta_2$  and  $\alpha_V\beta_3$ , with divergence beginning at the  $\beta$ -ankle loop that separates I-EGF4 from the  $\beta$ -tail (Figures 2H and 4D). The  $\beta$ -tail domain is well defined in multi-crystal averaged density (Figure 1C and F). Furthermore, the conformation of its CD loop is well defined, with unambiguous density for multiple large sidechains, and a strong anomalous signal for Met-660 at the tip of the CD loop (Figure 1C and F). The CD loop and the entire  $\beta$ -tail domain are far from the  $\beta$ I domain in the  $\beta_2$ -subunit (Supplementary Figure S4f); Met-660 is 35 Å away from the nearest residue in the  $\beta$ I domain  $\alpha$ 7-helix, Lys-340.

Why then would CD loop mutations be activating in  $\beta_2$  integrins? The  $\beta_2$ -tail CD loop is a major contributor to the contact with the preceding domain in the  $\beta$ -tail, I-EGF4

(Figure 4D; Supplementary Figure S4f). This contact substantially increases the size of the I-EGF4/ $\beta$ -tail interface from  $435 \text{ \AA}^2$  in  $\alpha_{\text{Ib}}\beta_3$  to  $744 \text{ \AA}^2$  in  $\alpha_X\beta_2$  (Table II). This interface is deeply buried in the cleft occupied by the lower  $\beta$ -leg, between the hybrid domain on one side and the calf-2 domain in the other. Thus, mutation of the  $\beta_2$ -tail CD loop is predicted to greatly destabilize the orientation between the I-EGF4 and  $\beta$ -tail domains in the bent conformation. Thus, it is also likely to destabilize the buried conformation of the lower  $\beta$ -leg, and result in integrin extension. Thus, the deadbolt hypothesis has been disproved for the integrin for which it was originally proposed,  $\alpha_V\beta_3$  (Zhu *et al*, 2007, 2008), and the single CD loop mutational study interpreted in favour of the deadbolt hypothesis, carried out in a  $\beta_2$  integrin (Gupta *et al*, 2007), has now been shown not to support this hypothesis, and to instead support activation by integrin extension.

### Signal transmission between the $\beta$ I and $\alpha$ I domains in integrin activation

How is activation transmitted to the  $\alpha$ I domain?  $\alpha$ I-less integrins have two distinct conformational states of the  $\beta$ I domain, in the closed and open headpieces. The headpiece is closed in the bent-closed and extended-closed conformations, and open in the extended-open conformation (Luo *et al*, 2007). Similarly, EM shows that when  $\alpha_X\beta_2$  extends, its headpiece can remain closed (Figure 2E), as seen in the bent crystal structure or can open, with the hybrid domain swung out (Figure 2F) (Nishida *et al*, 2006). In ligand binding in  $\alpha$ I-less integrins, the open state of the  $\beta$ I domain MIDAS  $\text{Mg}^{2+}$  ion coordinates the Asp sidechain in ligands such as Arg-Gly-Asp (Luo *et al*, 2007; Springer *et al*, 2008). In contrast to such binding to an extrinsic ligand, the  $\beta$ I MIDAS of  $\alpha$ I integrins may bind an intrinsic ligand, that is to an invariant Glu residue that corresponds to the first residue in the  $\alpha$ I C-linker,  $\alpha_X$  Glu-318 (Figure 3A and B). Mutation of this Glu abolishes integrin activation (Huth *et al*, 2000; Alonso *et al*, 2002). In contrast, when mutation of this Glu to Cys is combined with mutation of  $\beta_2$ I MIDAS-loop residue Ala-210 to Cys, an intersubunit disulfide bond forms, and ligand binding is constitutively activated (Yang *et al*, 2004).

In our structure,  $\alpha_X$  Glu-318 does not bind the  $\beta_2$ I MIDAS, consistent with the finding that both the  $\alpha_X$  and  $\beta_2$ I domains are in the closed, low-affinity conformations. However, the orientation of the  $\alpha_X$ I domain with respect to the remainder of the ectodomain, and of  $\alpha_X$  Glu-318 with respect to the  $\beta_2$ I MIDAS lends credence to the intrinsic-ligand hypothesis (Figure 3A and B). The  $\alpha_X$ I domain is oriented such that the C-linker is at the interface between the  $\beta$ -propeller and  $\beta$ I domains, where  $\alpha$ I-less integrins bind ligands. Indeed,  $\alpha_X$  C-linker residues 325–329 occupy a position at this interface similar to that of the fibrinogen peptide at the  $\alpha_{\text{Ib}}\beta_3$  recognition interface (Springer *et al*, 2008) (Figure 3D). In the two  $\alpha_X\beta_2$  molecules with density for the  $\alpha_X$ I domain, the last residue with significant interaction with the  $\alpha_X$ I domain is  $\alpha$ 7-helix residue Ile-317, which is buried in a hydrophobic region at the base of the  $\alpha$ I domain. Multi-crystal averaging density for the  $\alpha_X$ I domain shows continuous  $1 \sigma$  backbone density up to residue 317,  $0.6 \sigma$  density for residues 318 and 319, less density thereafter, and resumption again of  $1 \sigma$  backbone density at residue 328 (Figure 1B and E). On the basis of somewhat better  $2F_o - F_c$  density, the sidechain of Glu-318 is

modelled as pointing towards the  $\beta_2$ I MIDAS, 16–19  $\text{\AA}$  away in the two  $\alpha_X\beta_2$  molecules. The C $\beta$  atoms of  $\alpha_X$  Glu-318 and  $\beta_2$  Ala-210, which when mutated to Cys form an activating intersubunit disulfide bond (Yang *et al*, 2004), are 14–18  $\text{\AA}$  apart. Thus,  $\alpha_X$  Glu-318 is poised to coordinate the  $\beta_2$  MIDAS on conformational rearrangement.

As residue Ile-317 is buried in a hydrophobic pocket in the  $\alpha_X$ I domain, and continuous backbone density is present through this residue, the position of  $\alpha_X$  residue Glu-318 is highly constrained by the position of the  $\alpha_X$ I domain and its  $\alpha$ 7-helix. Owing to the flexible connection of the  $\alpha_X$ I domain to the  $\beta$ -propeller domain, particularly at the C-linker, rigid body motion of the  $\alpha_X$ I domain relative to the  $\beta$ -propeller domain can bring  $\alpha_X$  Glu-318 closer to the  $\beta_2$  MIDAS. However, clashes between the domains would occur before the  $\alpha_X$  Glu-318 sidechain could coordinate the  $\beta_2$  MIDAS. It thus appears that axial displacement of the  $\alpha_X$ I domain  $\alpha$ 7-helix would be required for MIDAS engagement.

Flexibility of  $\alpha$ I domains had not been noted in an earlier EM study, and it had been thought that a ‘relatively firm interface between the  $\alpha$ I and  $\beta$ -propeller domains... would favour downward displacement of the  $\alpha$ 7-helix, rather than tilting of the  $\alpha$ I domain’ on engagement of the  $\alpha$ I Glu residue with the  $\beta$ I MIDAS (Nishida *et al*, 2006) (Figure 6A and B). This postulated rigid connection presented a quandary—how could a two-position switch in the  $\beta$ I domain connect to a three-position switch in the  $\alpha$ I domain? Structures of isolated integrin  $\alpha$ I domains have shown three conformational states, termed closed, intermediate and open (Luo *et al*, 2007). Relative to the closed conformation of the  $\alpha$ I domain seen here in bent  $\alpha_X\beta_2$ , intermediate and open  $\alpha$ I domains have C-terminal  $\alpha$ 7-helices that are displaced one and two turns along the helical axis in the C-terminal direction, respectively, and have intermediate and high affinity for ligand (Shimaoka *et al*, 2003; Jin *et al*, 2004).

The flexibility of the  $\alpha$ I domain revealed in this study resolves this conundrum. One-turn and two-turn displacements of the  $\alpha$ 7-helix in the intermediate and open states, respectively, may each be sufficient for binding of Glu-318 to the  $\beta$ I MIDAS, when combined with some helix unwinding and with different orientations of the  $\alpha$ I domain with respect to the  $\beta$ -propeller and  $\beta$ I domains (Figure 6C–E). Moreover, strain energy stored in domain tilting or helix unwinding required for Glu-318 to reach the  $\beta$  MIDAS in the intermediate  $\alpha$ I state with one-turn  $\alpha$ -helix displacement (Figure 6D) could be released on conversion to two-turn  $\alpha$ -helix displacement in the open  $\alpha$ I state, and compensate for the higher energy of the open  $\alpha$ I MIDAS (Figure 6E). On the basis of crystal structure studies on intermediate state  $\alpha$ I domains (Shimaoka *et al*, 2003), initial coupling between the  $\beta$ I and  $\alpha$ I domains might stabilize the intermediate  $\alpha$ I domain state with a closed MIDAS (Figure 6D), which on ligand binding would convert to the open  $\alpha$ I state with an open MIDAS (Figure 6E). This flexibility enables fine-tuning of integrin adhesiveness. These ideas are important to test with further structures of  $\alpha$ I integrins in active states.

### Other functions for $\alpha$ I domain flexibility

Flexibility of the  $\alpha$ I domain may also be important in integrin mechanobiology. The actin cytoskeleton binds to the integrin  $\beta$ -subunit, and exerts a tensile force between the  $\beta$ -subunit cytoplasmic domain and ligand-binding site of  $\alpha$ I-



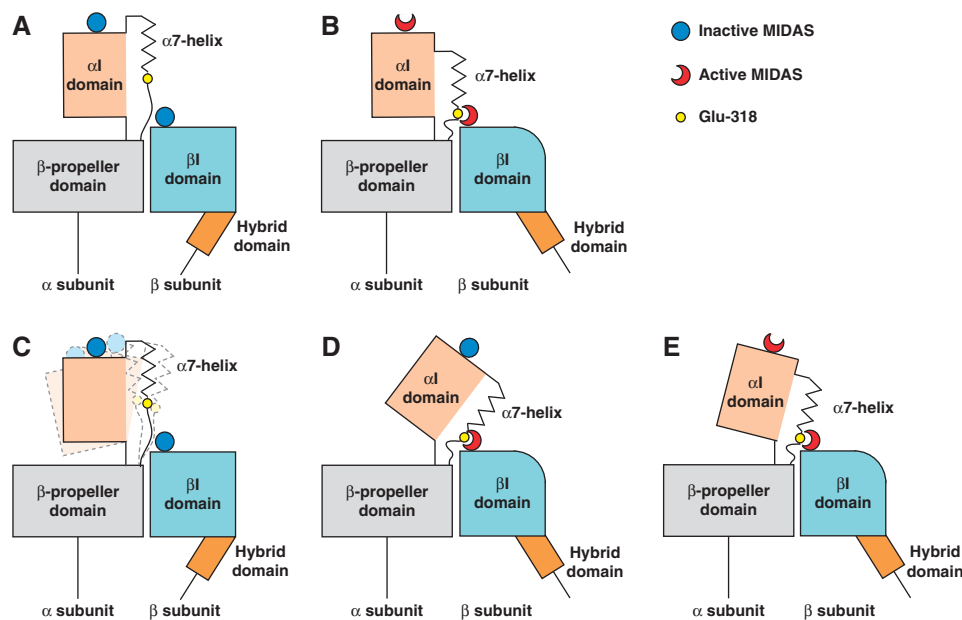


**Figure 6** Communication of allostery between  $\alpha$ I and  $\beta$ I domains. (A, B) Previous model with firm interface between the  $\alpha$ -subunit I and  $\beta$ -propeller domains (Nishida *et al*, 2006). There should be a 1:1 correspondence between  $\alpha$ I and  $\beta$ I domain conformational states according to this model (A, closed; B, open). (C–E) Current model, with a flexible interface between the  $\alpha$ -subunit I and  $\beta$ -propeller domains. This enables three states of the  $\alpha$ I domain to couple to two states of the  $\beta$ I domain. (C) When the  $\alpha$ I and  $\beta$ I domains are each in the closed state, the  $\alpha$ I domain is flexible. (D, E) Both the intermediate state  $\alpha$ I domain, with its MIDAS closed and  $\alpha$ 7-helix displaced one turn (D), and the open state  $\alpha$ I domain, with its MIDAS open and  $\alpha$ 7-helix displaced two turns (E), can couple to the open  $\beta$ I domain. The greater tilting of the  $\alpha$ I domain in (D) suggests greater strain than in (E). Lessening of this strain in (E) would help compensate for the higher energy of the open  $\alpha$ I MIDAS.

less integrins that stabilizes the open, high affinity state of the headpiece (Zhu *et al*, 2008). A tensile force on the C-terminal  $\alpha$ 7-helix, but not N-terminal  $\beta$ -strand, of isolated, ligand-bound  $\alpha$ I domains stabilizes the open  $\alpha$ I domain state (Astrof *et al*, 2006). Tensile force exerted between the ligand-binding site of the  $\alpha$ I domain and the  $\beta$ -subunit cytoplasmic domain in an intact, activated integrin would be transmitted through the N-linker to the  $\beta$ -propeller domain and through the C-linker to the  $\beta$ I domain MIDAS, and favour pivoting of the  $\alpha$ I domain to an orientation different than that captured in crystals, in which the tensile force would be better aligned with the  $\alpha$ 7-helix axis, facilitating mechanochemical stabilization of the open  $\alpha$ I domain state (Zhu *et al*, 2008).

The flexibility of the  $\alpha$ I domain revealed here, together with its capacity for allostery, may be the key features that account for the appearance of  $\alpha$ I integrins in chordates and their expansion in mammals to become half of all integrin  $\alpha$ -subunits. The combined  $\beta$ -propeller and  $\beta$ I domain ligand-binding unit in  $\alpha$ I-less integrins is far bulkier and less flexible than the  $\alpha$ I domain, and often binds flexible ligands such as Arg-Gly-Asp. CR4 recognizes iC3b covalently linked to pathogen surfaces. The flexibility of the  $\alpha$ I domain in  $\alpha$ I integrins, and its extension above the integrin head, better suits  $\alpha$ I integrins for binding their less flexible and less accessible ligands, such as collagen fibrils ( $\alpha_1$ ,  $\alpha_2$ ,  $\alpha_{10}$ ,  $\alpha_{11}$ ), and ligands on cell surfaces ( $\alpha_L$ ,  $\alpha_M$ ,  $\alpha_X$ ,  $\alpha_D$ ,  $\alpha_E$ ).

## Materials and methods

### Production of soluble $\alpha_X\beta_2$ and crystallization

$\alpha_X\beta_2$  ectodomain constructs contained TEV protease sites, ACID-BASE coiled-coils, and Strep-II and His6 tags as described earlier (Nishida *et al*, 2006). An additional C-terminal disulfide was

introduced by altering the GTGG and DTSG linker sequences following  $\alpha_X$  and  $\beta_2$  (Nishida *et al*, 2006), to GCGG and DGCG, respectively (Supplementary Figure S2a,b). CHO Lec 3.2.8.1 cells were cotransfected with these vectors and screened for single clones with high expression (Nishida *et al*, 2006). The clone with highest expression level (8 mg/l) was expanded and cultured in roller bottles at 37°C, and culture supernatants were collected every week. Soluble integrins were purified as described earlier (Nishida *et al*, 2006).

To obtain  $\alpha_X\beta_2$  protein for crystallization, purified recombinant protein was treated with His-tagged TEV protease (Invitrogen) at 250 U/mg and Endo H (Roche) at 0.1 U/mg at room temperature for 16 h, followed by re-pass-through the Ni-NTA column. The flow-through containing deglycosylated  $\alpha_X\beta_2$  protein was dialysed against and stored in TBS/Ca buffer (20 mM Tris-HCl pH7.5, 150 mM NaCl, 5 mM CaCl<sub>2</sub>), and further purified by Superdex 200 (Amersham Biosciences, Piscataway, NJ) size-exclusion chromatography in TBS buffer (20 mM Tris-HCl pH7.5, 150 mM NaCl). Purified  $\alpha_X\beta_2$  was concentrated to 8 mg/ml, and screened for crystallization conditions using the Topaz crystallizer (Fluidigm, South San Francisco, CA). Lead conditions were optimized using hanging drop vapour diffusion.

Three crystal lattices were obtained. The final optimized well solution(s) for lattice A is 0.55 M tri-sodium citrate and 0.1 M imidazole, pH 6.5, for lattice C are 0.915 M sodium/potassium phosphate, pH 7.2 or 32% Tacimate and 0.1 M Bis-Tris Propane, pH 7.0. Crystals with lattice B were obtained by soaking the crystals with lattice A into 0.55 M tri-sodium citrate, 0.05 M MgCl<sub>2</sub>, 0.1 mM ICAM-1 domain 3 and 0.1 M imidazole, pH 6.5.

To prepare Se-Met  $\alpha_X\beta_2$ , cells were washed with phosphate-buffered saline supplemented with 1% dialysed FCS, incubated with methionine-free  $\alpha$ -MEM (SAFC Biosciences) supplemented with 50 mg/l L-Se-Met (Sigma) and 10% dialysed FCS, replaced with the same medium after 6 h, and cultured for 3–4 days. Se-Met  $\alpha_X\beta_2$  was purified, deglycosylated, obtained in about 60% yield as native material, and crystallized in lattices A and C as described above.

### X-ray crystallography

Diffraction data collected at APS ID-23 (Table I) were processed with XDS (Kabsch, 2001). [TaBr<sub>12</sub>(H<sub>2</sub>O)<sub>6</sub>]<sup>2+</sup>Br<sup>−</sup>OH<sup>−</sup>·5H<sub>2</sub>O was

soaked into crystals with lattice A. Four tantalum bromide clusters were found by SOLVE (Terwilliger and Berendzen, 1999), and initial phases were obtained from Ta SAD (Table I) data for lattice A. The electron density map of lattice A after density modification by RESOLVE (Terwilliger, 2000) showed a clear boundary between protein and solvent. However, no secondary structural features were revealed. To determine the Se substructure of the Se-derivative crystal, the anomalous signals from the peak wavelength of Se-MAD data for lattice A (Table I) were combined with the initial phases from Ta SAD data for lattice A to calculate an anomalous Fourier map. The top 12 peaks were picked as the starting Se sites for SOLVE. 78 of 100 Se atoms were identified and a set of phases from Se-MAD data for lattice A was generated by SOLVE. The phases were then transferred to the high-resolution native data for lattice A. Density modification was carried out by RESOLVE to improve the electron density map and extend the phases to higher resolution. The starting model for each domain of integrin  $\alpha_x\beta_2$  was built by homology modelling program MODELLER (Sali and Blundell, 1993) using corresponding domains from integrin  $\alpha_{IIb}\beta_3$  and  $\alpha_V\beta_3$  structures as templates. Homology models of the  $\beta$ -propeller domain, thigh domain, and  $\beta$ I domain could be placed into the density-modified map by MOLREP (Vagin and Teplyakov, 1997) in CCP4 (Bailey, 1994). The other domains were placed into the map manually. A crude model of integrin  $\alpha_x\beta_2$  was obtained after rigid body refinement by PHENIX.REFINE (Adams *et al*, 2002) with each domain as one rigid body. Molecular replacement solutions for lattice B and C were solved by PHASER (McCoy *et al*, 2007) using the crude model of integrin  $\alpha_x\beta_2$  in lattice A as the searching model. The molecular replacement phases for lattice C combined with the anomalous signals from the peak wavelength of Se-MAD data for lattice C (Table I) were used to determine the Se substructure of Se-derivative crystal with lattice C; 32 of 50 Se atoms were identified and a new set of phases for lattice C was generated by SOLVE. Phases for lattice C were then transferred to the high-resolution native data for lattice C. To improve the phases and extend them to higher resolution, multi-crystal averaging (three crystals in total: lattice A, B, C), multi-domain averaging (with a separate mask for each of the 12 domains resolved in 8 molecules and 13 domains resolved in 2 molecules) along with solvent flattening and histogram matching were performed by DMMULTI (Cowtan, 1994) from the CCP4 suite. The mask for each domain was calculated by NCSMASK in CCP4. As the domain-domain angles are quite different in each molecule (Figure 2H), the NCS matrices for each domain between molecules and crystals were computed by LSQKAB in CCP4. Rigid body refinements were carried out by PHENIX.REFINE for each lattice based on the averaged maps. The new models for each lattice were then used to calculate a set of new NCS matrices for the next cycle of DMMULTI. These steps were cycled three times. Model building in COOT (Emsley and Cowtan, 2004) was based on multi-crystal, multi-domain averaging electron density maps. The phases for lattice A

and C after averaging were subsequently used in MLHL refinement of lattice A and C using PHENIX.REFINE. Refinement of lattice B was carried out with no experimental phases. NCS restraints and TLS groups were used in refinement. To stabilize the refinement at such low resolution, hydrogen-bond restraints for secondary structural features were applied in the early stage of the refinement. The secondary structure assignment was based on integrin sequence and structural alignment. These restraints were completely omitted later in refinement. The sequence to structure register was confirmed or adjusted using Se anomalous maps. The sequence register at the two junctions between the  $\beta$ -propeller domain and  $\alpha$ -I domain was confirmed by several methods. First, the disulfide bond between Cys-97 and Cys-126 was clear in electron density maps (Figure 1E). Second, the Phe-328 sidechain had clear density, and the anomalous signal for SeMet-332 was clear (Figure 1E). Third, the anomalous signals from four SeMet residues in the  $\alpha_x$ I domain confirmed its orientation (Figure 1A and B). Validation and Ramachandran statistics used MOPROBITY (Davis *et al*, 2007).

#### Interdomain angle calculation

Every tandem domain pair from molecules being compared was superimposed on the first tandem domain using SUPER command in Pymol. The matrix generated by a second superposition on the second tandem domain was obtained with GET\_OBJECT\_MATRIX command in Pymol and used to calculate the  $\kappa$  angle in polar angles.

#### Negative stain EM of $\alpha_x\beta_2$

$\alpha_x\beta_2$  constructs treated with or without TEV protease were purified on Superdex 200 HR equilibrated with TBS, 1 mM CaCl<sub>2</sub>, 1 mM MgCl<sub>2</sub>. Peak fractions were adsorbed to glow discharged carbon-coated copper grids, stained with uranyl formate, and images acquired with an FEI Tecnai 12 electron microscope at 120 kV at a nominal magnification of  $\times 67000$ ; 2000–6000 particles were interactively collected, and subjected to 10 cycles of multi-reference alignment and k-means classification with SPIDER (Frank *et al*, 1996) as described (Nishida *et al*, 2006).

#### Supplementary data

Supplementary data are available at *The EMBO Journal* Online (<http://www.embojournal.org>).

## Acknowledgements

The work is supported by NIH grant AI 72765.

## Conflict of interest

The authors declare that they have no conflict of interest.

## References

- Adams PD, Grosse-Kunstleve RW, Hung LW, Ioerger TR, McCoy AJ, Moriarty NW, Read RJ, Sacchettini JC, Sauter NK, Terwilliger TC (2002) PHENIX: building new software for automated crystallographic structure determination. *Acta Crystallogr D Biol Crystallogr* **58**: 1948–1954
- Alonso JL, Essafi M, Xiong JP, Stehle T, Arnaout MA (2002) Does the integrin  $\alpha$ A domain act as a ligand for its  $\beta$ A domain? *Curr Biol* **12**: R340–R342
- Astrof NS, Salas A, Shimaoka M, Chen JF, Springer TA (2006) Importance of force linkage in mechanobiology of adhesion receptors. *Biochemistry* **45**: 15020–15028
- Bailey S (1994) The CCP4 suite—programs for protein crystallography. *Acta Crystallogr* **50**: 760–763
- Beglova N, Blacklow SC, Takagi J, Springer TA (2002) Cysteine-rich module structure reveals a fulcrum for integrin rearrangement upon activation. *Nat Struct Biol* **9**: 282–287
- Cowtan K (1994) An automated procedure for phase improvement by density modification. Joint CCP4 and ESF-EACBM. *News Protein Crystallogr* **31**: 34–38
- Davis IW, Leaver-Fay A, Chen VB, Block JN, Kapral GJ, Wang X, Murray LW, Arendall III WB, Snoeyink J, Richardson JS, Richardson DC (2007) MOLPROBITY: all-atom contacts and structure validation for proteins and nucleic acids. *Nucleic Acids Res* **35**: W375–W383
- Emsley P, Cowtan K (2004) Coot: model-building tools for molecular graphics. *Acta Crystallogr* **60**: 2126–2132
- Frank J, Radermacher M, Penczek P, Zhu J, Li Y, Ladjadj M, Leith A (1996) SPIDER and WEB: processing and visualization of images in 3D electron microscopy and related fields. *J Struct Biol* **116**: 190–199
- Gupta V, Gylling A, Alonso JL, Sugimori T, Ianakiev P, Xiong JP, Arnaout MA (2007) The beta-tail domain (betaTD) regulates physiologic ligand binding to integrin CD11b/CD18. *Blood* **109**: 3513–3520
- Huth JR, Olejniczak ET, Mendoza R, Liang H, Harris EA, Lupher Jr ML, Wilson AE, Fesik SW, Staunton DE (2000) NMR and mutagenesis evidence for an I domain allosteric site that regulates lymphocyte function-associated antigen 1 ligand binding. *Proc Natl Acad Sci USA* **97**: 5231–5236
- Jin M, Andricioaei I, Springer TA (2004) Conversion between three conformational states of integrin I domains with a C-terminal pull spring studied with molecular dynamics. *Structure* **12**: 2137–2147

- Kabsch W (2001) Chapter 25.2.9 XDS. In: Rossmann MG, Arnold E (eds). *International Tables for Crystallography*. Kluwer Academic Publishers: Dordrecht: 730–734
- Kalomiris EL, Collier BS (1985) Thiol-specific probes indicate that the beta-chain of platelet glycoprotein Ib is a transmembrane protein with a reactive endofacial sulfhydryl group. *Biochemistry* **24**: 5430–5436
- Kamata T, Tieu KK, Tarui T, Puzon-McLaughlin W, Hogg N, Takada Y (2002) The role of the CPNKEKEC sequence in the beta(2) subunit I domain in regulation of integrin alpha(L)beta(2) (LFA-1). *J Immunol* **168**: 2296–2301
- Lau TL, Kim C, Ginsberg MH, Ulmer TS (2009) The structure of the integrin  $\alpha_{IIb}\beta_3$  transmembrane complex explains integrin transmembrane signalling. *EMBO J* **9**: 1351–1361
- Lo Conte L, Chothia C, Janin J (1999) The atomic structure of protein-protein recognition sites. *J Biol Chem* **285**: 2177–2198
- Lu C, Ferzly M, Takagi J, Springer TA (2001a) Epitope mapping of antibodies to the C-terminal region of the integrin  $\beta_2$  subunit reveals regions that become exposed upon receptor activation. *J Immunol* **166**: 5629–5637
- Lu C, Shimaoka M, Zang Q, Takagi J, Springer TA (2001b) Locking in alternate conformations of the integrin  $\alpha_L\beta_2$  I domain with disulfide bonds reveals functional relationships among integrin domains. *Proc Natl Acad Sci USA* **98**: 2393–2398
- Luo B-H, Carman CV, Springer TA (2007) Structural basis of integrin regulation and signaling. *Annu Rev Immunol* **25**: 619–647
- Luo B-H, Takagi J, Springer TA (2004) Locking the  $\beta_3$  integrin I-like domain into high and low affinity conformations with disulfides. *J Biol Chem* **279**: 10215–10221
- McCoy AJ, Grosse-Kunstleve RW, Adams PD, Winn MD, Storoni LC, Read RJ (2007) Phaser crystallographic software. *J Appl Crystallogr* **40**: 658–674
- Nishida N, Xie C, Shimaoka M, Cheng Y, Walz T, Springer TA (2006) Activation of leukocyte  $\beta_2$  integrins by conversion from bent to extended conformations. *Immunity* **25**: 583–594
- O'Neill S, Robinson A, Deering A, Ryan M, Fitzgerald DJ, Moran N (2000) The platelet integrin  $\alpha_{IIb}\beta_3$  has an endogenous thiol isomerase activity. *J Biol Chem* **275**: 36984–36990
- Sali A, Blundell TL (1993) Comparative protein modelling by satisfaction of spatial restraints. *J Mol Biol* **234**: 779–815
- Shi M, Foo SY, Tan SM, Mitchell EP, Law SK, Lescar J (2007) A structural hypothesis for the transition between bent and extended conformations of the leukocyte  $\beta_2$  integrins. *J Biol Chem* **282**: 30198–30206
- Shi M, Sundramurthy K, Liu B, Tan SM, Law SK, Lescar J (2005) The crystal structure of the plexin-semaphorin-integrin domain/hybrid domain/I-EGF1 segment from the human integrin  $\beta_2$  subunit at 1.8-Å resolution. *J Biol Chem* **280**: 30586–30593
- Shimaoka M, Xiao T, Liu J-H, Yang Y, Dong Y, Jun C-D, McCormack A, Zhang R, Joachimiak A, Takagi J, Wang J-h, Springer TA (2003) Structures of the  $\alpha_L$  I domain and its complex with ICAM-1 reveal a shape-shifting pathway for integrin regulation. *Cell* **112**: 99–111
- Springer TA, Wang J-h (2004) The three-dimensional structure of integrins and their ligands, and conformational regulation of cell adhesion. *Adv Protein Chem* **68**: 29–63
- Springer TA, Zhu J, Xiao T (2008) Structural basis for distinctive recognition of fibrinogen by the platelet integrin  $\alpha_{IIb}\beta_3$ . *J Cell Biol* **182**: 791–800
- Takagi J, Beglova N, Yalamanchili P, Blacklow SC, Springer TA (2001) Definition of EGF-like, closely interacting modules that bear activation epitopes in integrin  $\beta$  subunits. *Proc Natl Acad Sci USA* **98**: 11175–11180
- Tang RH, Tng E, Law SK, Tan SM (2005) Epitope mapping of monoclonal antibody to integrin  $\alpha_L\beta_2$  hybrid domain suggests different requirements of affinity states for intercellular adhesion molecules (ICAM)-1 and ICAM-3 binding. *J Biol Chem* **280**: 29208–29216
- Terwilliger TC (2000) Maximum-likelihood density modification. *Acta Crystallogr D Biol Crystallogr* **56**: 965–972
- Terwilliger TC, Berendzen J (1999) Automated MAD and MIR structure solution. *Acta Crystallogr D Biol Crystallogr* **55**: 849–861
- Tng E, Tan SM, Ranganathan S, Cheng M, Law SK (2004) The integrin  $\alpha_L\beta_2$  hybrid domain serves as a link for the propagation of activation signal from its stalk regions to the I-like domain. *J Biol Chem* **279**: 54334–54339
- Vagin A, Teplyakov A (1997) MOLREP: an automated program for molecular replacement. *J Appl Crystallogr* **30**: 1022–1025
- Vorup-Jensen T, Carman CV, Shimaoka M, Schuck P, Svitol J, Springer TA (2005) Exposure of acidic residues as a danger signal for recognition of fibrinogen and other macromolecules by integrin  $\alpha_X\beta_2$ . *Proc Natl Acad Sci USA* **102**: 1614–1619
- Vorup-Jensen T, Ostermeier C, Shimaoka M, Hommel U, Springer TA (2003) Structure and allosteric regulation of the  $\alpha_X\beta_2$  integrin I domain. *Proc Natl Acad Sci USA* **100**: 1873–1878
- Xiao T, Takagi J, Wang J-h, Collier BS, Springer TA (2004) Structural basis for allostery in integrins and binding of fibrinogen-mimetic therapeutics. *Nature* **432**: 59–67
- Xie C, Shimaoka M, Xiao T, Schwab P, Klickstein LB, Springer TA (2004) The integrin  $\alpha$  subunit leg extends at a  $Ca^{2+}$ -dependent epitope in the thigh/genu interface upon activation. *Proc Natl Acad Sci USA* **101**: 15422–15427
- Xiong J-P, Stehle T, Diefenbach B, Zhang R, Dunker R, Scott DL, Joachimiak A, Goodman SL, Arnaout MA (2001) Crystal structure of the extracellular segment of integrin  $\alpha_V\beta_3$ . *Science (NY)* **294**: 339–345
- Xiong JP, Mahalingham B, Alonso JL, Borrelli LA, Rui X, Anand S, Hyman BT, Rysiok T, Muller-Pompalla D, Goodman SL, Arnaout MA (2009) Crystal structure of the complete integrin  $\alpha_V\beta_3$  ectodomain plus an  $\alpha/\beta$  transmembrane fragment. *J Cell Biol* **186**: 589–600
- Xiong JP, Stehle T, Goodman SL, Arnaout MA (2003) New insights into the structural basis of integrin activation. *Blood* **102**: 1155–1159
- Xiong JP, Stehle T, Zhang R, Joachimiak A, Frech M, Goodman SL, Arnaout MA (2002) Crystal structure of the extracellular segment of integrin  $\alpha_V\beta_3$  in complex with an Arg-Gly-Asp ligand. *Science (NY)* **296**: 151–155
- Yan B, Smith JW (2001) Mechanism of integrin activation by disulfide bond reduction. *Biochemistry* **40**: 8861–8867
- Yang W, Shimaoka M, Salas A, Takagi J, Springer TA (2004) Inter-subunit signal transmission in integrins by a receptor-like interaction with a pull spring. *Proc Natl Acad Sci USA* **101**: 2906–2911
- Zang Q, Lu C, Huang C, Takagi J, Springer TA (2000) The top of the I-like domain of the integrin LFA-1  $\beta$  subunit contacts the  $\alpha$  subunit  $\beta$ -propeller domain near  $\beta$ -sheet 3. *J Biol Chem* **275**: 22202–22212
- Zang Q, Springer TA (2001) Amino acid residues in the PSI domain and cysteine-rich repeats of the integrin  $\beta_2$  subunit that restrain activation of the integrin  $\alpha_X\beta_2$ . *J Biol Chem* **276**: 6922–6929
- Zhu J, Boylan B, Luo B-H, Newman PJ, Springer TA (2007) Tests of the extension and deadbolt models of integrin activation. *J Biol Chem* **16**: 11914–11920
- Zhu J, Luo BH, Barth P, Schonbrun J, Baker D, Springer TA (2009) The structure of a receptor with two associating transmembrane domains on the cell surface: integrin  $\alpha_{IIb}\beta_3$ . *Mol Cell* **34**: 234–249
- Zhu J, Luo BH, Xiao T, Zhang C, Nishida N, Springer TA (2008) Structure of a complete integrin ectodomain in a physiologic resting state and activation and deactivation by applied forces. *Mol Cell* **32**: 849–861



## Supplementary Materials

### Methods.

**Waters and metals.** Density for the  $\alpha$ I MIDAS and  $\beta$ I ADMIDAS metals was clearly visible. Although separate density for water molecules is not present at the resolution obtained, waters were included near these metals when they were in density, or when they improved the geometry of metal – protein coordination during refinement. Density was present for metals in the  $\beta$ -propeller  $\text{Ca}^{2+}$ -binding  $\beta$ -hairpin loops; although this density was not separate from that for surrounding metal-coordinating residues, metals were included, because otherwise metal-coordinating oxygens came too close to one another after refinement.

### Results.

**The genu.** The connection between the thigh and the genu differs markedly in conformation in  $\alpha_X$  compared to  $\alpha_{IIb}$  and  $\alpha_V$  and helps account for the closer interaction between the thigh and calf-1 domains in  $\alpha_X$ . The five residues in the thigh domain preceding the genu, where the conformational differences occur, have a different consensus sequence in  $\alpha_X$  and other  $\alpha$ I domain integrins than in  $\alpha_{IIb}$  and  $\alpha_V$  and other Arg-Gly-Asp binding integrins (Fig. S5a), suggesting that the differences in thigh/calf-1 orientation between  $\alpha_X$  and  $\alpha_{IIb}$  described here are characteristic for these classes of integrins. Mutations of the genu in the  $\alpha_L$ -subunit, including Ca-binding residues, decrease exposure of activation-dependent epitopes and decrease ligand binding (Fig. S5b,c), suggesting that these mutations stabilize the bent conformation. These findings

suggest that Ca binds with higher affinity to the extended genu than the bent genu of  $\alpha$ I integrins, and are consistent with the lack of a Ca-binding conformation of the genu found here in crystals. Antibodies that recognize the active state of  $\alpha_L\beta_2$  map to residues buried on the thigh domain by the calf-1 domain (Fig. 2a,b); furthermore, binding of these antibodies also requires  $\text{Ca}^{2+}$  and is disrupted by mutation of putative Ca-binding residues in the genu (Xie et al, 2004).

**The headpiece and Lys finger.** In the headpiece of  $\alpha_X\beta_2$ , the  $\beta$ -propeller domain and  $\beta$ I domain associate over an extensive interface with an inter-domain orientation essentially identical to that in  $\alpha_{IIb}\beta_3$ . The  $\beta$ -propeller has seven  $\beta$ -sheets or blades tightly packed together around a pseudosymmetry axis. The  $\beta_2$  I domain caps one hub of the  $\beta$ -propeller. Although the interfaces are overall similar, in  $\alpha_X\beta_2$  compared to  $\alpha_V\beta_3$  (Xiong et al, 2001) and  $\alpha_{IIb}\beta_3$  (Zhu et al, 2008), a Lys rather than an Arg finger inserts into the  $\beta$ -propeller pseudosymmetry axis, and interactions of the fingertip residue with hub residues are less extensive (Fig. S7).

## Supplementary Figure Legends

**Figure S1. Structure-based sequence alignments.** **a**, alignment of  $\alpha_X$  with  $\alpha_{Ib}$  (Zhu et al, 2008) and  $\alpha_V$  (Xiong et al, 2004). **b**, Alignment of  $\beta_2$  with  $\beta_3$  (Zhu et al, 2008).

Domains were separately superimposed using SSM (Krissinel & Henrick, 2004).

Structurally equivalent residues are in upper case and otherwise in lower case. Residues absent from structures are in italics.  $\alpha$  or  $3_{10}$ -helices are highlighted in cyan and  $\beta$ -strands in pink.

**Figure S2. Ectodomain constructs and all class averages from negative stain EM.** **a**,

Schematic of integrin  $\alpha_X\beta_2$  ectodomain constructs with a C-terminal linker containing a TEV protease cleavage site and a coiled-coil. **b**, Schematic of integrin  $\alpha_X\beta_2$  ectodomain

constructs with an additional disulfide bond between GCG sequences following the ectodomain C-termini and preceding the linker. **c**,  $\alpha_X\beta_2$  construct as in **b** with C-terminal

GCG disulfide and coiled-coil. **d**,  $\alpha_X\beta_2$  construct with C-terminal coiled-coil as in **a**. **e**,

The same construct as in **b** and **c** with TEV cleavage to remove the C-terminal coiled-

coil. **f**, The same construct as in **a** and **d**, with TEV cleavage to remove the C-terminal coiled-coil.

**Figure S3. Superpositions of domains.** **a**, Relative orientation between Calf-2 domain and  $\beta$ -tail domain. The two domains from 10  $\alpha_X\beta_2$  molecules are superimposed on Calf-2 domain. **b**, superposition of the  $\alpha_X\beta_2$   $\alpha I$  domain and the isolated  $\alpha_X$  I domain (Vorup-Jensen et al, 2003), both of which show the closed conformation.



**Figure S4. Superpositions of  $\alpha_X\beta_2$  and  $\alpha_{IIB}\beta_3$  on their calf-2 domains, and the CD loop of the  $\beta$ -tail domain.** These superpositions emphasize the markedly different orientations of calf-2 in these integrins. In the orientations in a-c, the calf-2 domain is oriented so that its base would be approximately parallel to the plasma membrane, as a surrogate for orientation on the cell surface. **a**,  $\alpha_X\beta_2$  and **b**,  $\alpha_{IIB}\beta_3$  structure superimposed on calf 2. In **c**,  $\alpha_{IIB}\beta_3$  is rotated about  $50^\circ$  in the vertical axis of the page relative to **b**, revealing an overall orientation more similar that of  $\alpha_X\beta_2$  in **a**. **d-e**, views of **a** and **b** after rotation in the horizontal axis of the page, to show a bird's eye view looking down on the cell surface, and the significant differences in  $\alpha_{IIB}\beta_3$  and  $\alpha_X\beta_2$  orientation. **f-g**, The  $\beta$  subunits of  $\alpha_X\beta_2$  (**f**) and  $\alpha_V\beta_3$  (Xiong et al, 2004) (**g**), in identical orientations after superposition on the  $\beta$ -tail domain. The  $\beta$ 6-strand and  $\alpha$ 7-helix of the  $\beta$ I domain (red) are close to the  $\beta$  tail domain CD loop in  $\beta_3$  and not in  $\beta_2$ .

**Figure S5. The sequence at the genu and effect of mutation of putative genu  $\text{Ca}^{2+}$ -coordinating residues.** **a**, Sequence alignment of human integrin  $\alpha$  subunits around the genu. The disulfide-linked genu cysteine residues are highlighted in yellow. **b-c**, Effect of mutating putative genu  $\text{Ca}^{2+}$ -coordinating residues Asp-749 and Glu-787 in  $\alpha_L\beta_2$ . **b**. Effect on KIM127 and m24 activation epitope exposure. HEK 293T transient transfectants expressing WT or mutant  $\alpha_L\beta_2$  in medium containing 1mM  $\text{CaCl}_2$ /1mM  $\text{MgCl}_2$  or 2mM  $\text{MnCl}_2$  were stained with KIM127 or m24 mAbs and subjected to immunofluorescence flow cytometry. Expression of the activation-insensitive mAb MHM24 was not affected by  $\text{MnCl}_2$ . Data shows specific mean fluorescence intensity as

a percentage of MHM24-specific mean fluorescence intensity, and error bars represent the SD of three independent experiments. **c**, Effect of  $\alpha_L\beta_2$  genu  $\text{Ca}^{2+}$  binding site mutations on cell adhesion. Binding of fluorescently labeled HEK 293T transfectants to immobilized ICAM-1 was as described (Lu & Springer, 1997). Briefly, ICAM-1-IgG Fc fusion protein at 10  $\mu\text{g/ml}$  was immobilized on microtiter plates and blocked with 2% BSA. Binding of ICAM-1 was determined in HBS-BSA buffer (20mM Hepes, pH 7.5, 140 mM NaCl, 2 mg/ml glucose, 1% BSA) in the presence of divalent cations and/or activating antibody CBR LFA1/2 (10  $\mu\text{g/ml}$ ) or EDTA (5 mM) as indicated. After incubation at 37 °C for 30 min, unbound cells were washed off, and bound cells were quantitated.

**Figure S6. Sequence alignment.** **a**. Sequence alignment of human  $\alpha\text{I}$  integrin  $\alpha$  subunits around the  $\alpha\text{I}$  C-linker. The  $\alpha 7$  helix of the  $\alpha\text{I}$  domain is indicated above the sequence. The invariant Glu (E) is highlighted in cyan. **b**. Sequence alignment of  $\alpha_X$ ,  $\alpha_M$ ,  $\alpha_D$ , and  $\alpha_L$  around the linker between Calf-2 domain and TM domain.

**Figure S7.  $\beta$ -Propeller/ $\beta\text{I}$  domain interface.** **a**. Side view of the Arg or Lys finger of the  $\beta\text{I}$  domain and surrounding  $\beta$ -propeller domain residues. **b**, Top view.  $\alpha_X\beta_2$  residues are colored in cyan,  $\alpha_V\beta_3$  in silver and  $\alpha_{\text{Ib}}\beta_3$  in yellow.

## References

- Krissinel E, Henrick K (2004) Secondary-structure matching (SSM), a new tool for fast protein structure alignment in three dimensions. *Acta Crystallogr D Biol Crystallogr* **60**(Pt 12 Pt 1): 2256-2268
- Lu C, Springer TA (1997) The  $\alpha$  subunit cytoplasmic domain regulates the assembly and adhesiveness of integrin lymphocyte function-associated antigen-1 (LFA-1). *J Immunol* **159**: 268-278
- Vorup-Jensen T, Ostermeier C, Shimaoka M, Hommel U, Springer TA (2003) Structure and allosteric regulation of the  $\alpha_x\beta_2$  integrin I domain. *Proc Natl Acad Sci U S A* **100**: 1873-1878
- Xie C, Shimaoka M, Xiao T, Schwab P, Klickstein LB, Springer TA (2004) The integrin  $\alpha$  subunit leg extends at a  $\text{Ca}^{2+}$ -dependent epitope in the thigh/genu interface upon activation. *Proc Natl Acad Sci U S A* **101**: 15422-15427
- Xiong J-P, Stehle T, Diefenbach B, Zhang R, Dunker R, Scott DL, Joachimiak A, Goodman SL, Arnaout MA (2001) Crystal structure of the extracellular segment of integrin  $\alpha_v\beta_3$ . *Science (New York, NY)* **294**(5541): 339-345
- Xiong JP, Stehle T, Goodman SL, Arnaout MA (2004) A novel adaptation of the integrin PSI domain revealed from its crystal structure. *J Biol Chem* **279**: 40252-40254
- Zhu J, Luo BH, Xiao T, Zhang C, Nishida N, Springer TA (2008) Structure of a Complete Integrin Ectodomain in a Physiologic Resting State and Activation and Deactivation by Applied Forces. *Mol Cell* **32**(6): 849-861

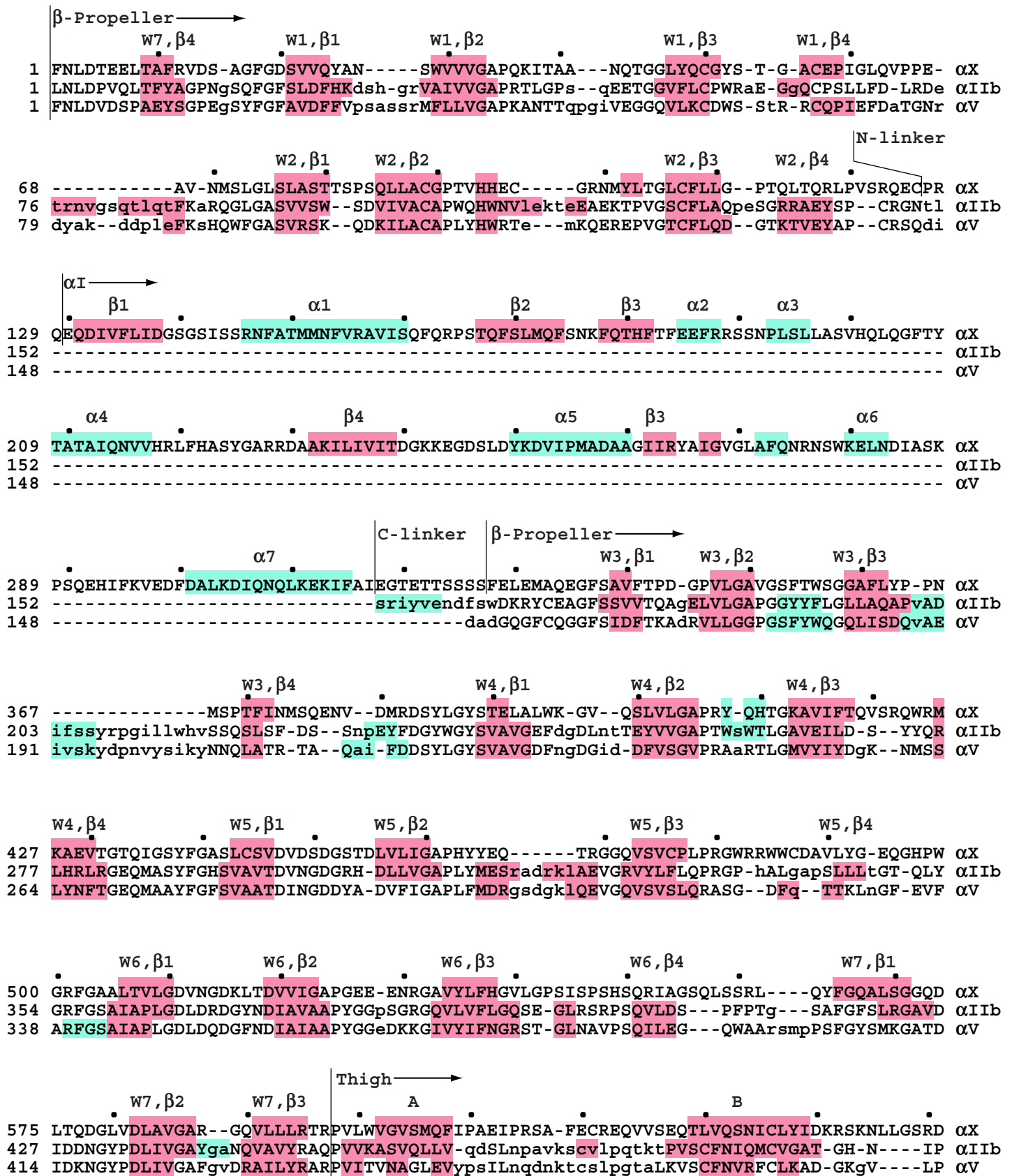


Fig. S1a\_p1

C D Z E F  
 652 LQSSVTLDLALDPGRL--SPRATFQETKNRSLSRVRL--GLKAHCENFNLLLPSC--VEDSVTPITLRLNFTLVGKPL αX  
 500 QKLSLNAELQLDRQKP-rqGRRVLLLGsqQAGTTLNLDlggkhsPICHTTMAFLRDEadFRDKLSPIVLSLNVSLPpTea αIIb  
 489 RKLNFQVELLLDKLKQkgaiRRALFLYsrSPSHSKNMTisrggLMQCEELIAYLRDEseFRDKLTPITIFMEYRLD-Yrt αV

G' G Genu A A' B C  
 725 LA-FRNLRPMLAADAQRYFTASLPFEKINCGADHICQDNLGISFSFPGLKSLVGSNLELNAEVMVWNDGEDSYGTTITFS αX  
 579 g---mapAVVLH--GDTHVQEQTTRIVLDCGEDDVCPQLQLTASVT-GSPLLVGADNVLELQMDAANELEGAYEAE LAVH αIIb  
 568 aadtgtlQPILNqfTPANISRQAHILLDCGEDNVCKPKLEVSVDSD-QKKIYIGDDNPLTLIVKAQNQEGEGAYEAE LIVS αV

D X Z E F  
 804 HPAGLSYRYVAEGQKQGQLRSLHLTCD SAPVGSQGTWSTSCRINHLIFRGAQITFLATFDVSPKAVLGDRLLLLTANVSS αX  
 653 LPQGAHYMRAL---snvegferLICNQQKENE---TRVVLCEL-GNPMKKNAQIGIAMLVSVGnleeageSVSFQLQIRS αIIb  
 647 IPLQADFIGV---vrnnealarLSCAFKTENQ---TRQVVC DL-GNPMKAGTQLLAGLRF SVHqqsemdTSVKFDLQIQS αV

G A A' B C  
 884 ENNTPRT-SKTTTFQLELPVKYAVYTVSSHEQFT-KYLN FSESE-----EKESHVAMHRYQVNNLGQRD-LPVSIN αX  
 726 KN--SQnpsSKIIVLLDVPVRAEAQVELRGN-SFPaSLVV-A-AEEGEREQNSLD SWGPKVEHTYELHNNPGPTvNGLHLS αIIb  
 720 SN--LFdkvSPVVS HKVDLAVLA AVEIRGV-SSPdHVFLpIpNwehkenpeteedVGPVVQHIYELRNNGPSSfSKAMLH αV

D X furin furin  
 952 FWVPVELNQ-EAVWMDVEVSH PQNPSLRCSSEKIAPPASDFLAHIQK----- αX  
 801 IHLPGQS-QpSDLLYildiappq-GG-LQCFPQPpvnplk---vdwGLPIPSPSPIHPAHHKRDRRQIFLPEPEEQPSRLQd αIIb  
 797 LQWPYKYnN-NTLLYilhydid-GP-MNCTSDMeinplrik--isslQTTEKNDTVAGQGERDH---LITKRDLALSEGd αV

Y Z E F G  
 998 NPVLDCSIAGCLRFRC DVPSFSVQEELDFTLKGNLSFGWVRQIL---QKKVSVSVSAEITFDTSVYSQLPGQEAFMRAQT αX  
 875 pvLVSCDSAPCTVVQCDLQEMARGQ RAMVTVLAflwlp slyqrp---LDQFVLQSHAWFNVSslpyavpplslprGEAQV αIIb  
 869 ihTLGCGVAQCLKIVCQVGRLDRGKSAILYVKSllwte-tfmnkenqNHSYSLKSSASFNViefpyknlpieditNSTLV αV

Linker Transmembrane Cytoplasmic  
 1075 TTVLEKYKVH---NPTPLIVGSSIGLLLLALITAVLYKVGFFKRQYKEMME-EANGQIAPENGQTQTPSPSPSEK αX  
 952 WTQLLRAL EERA--IPIWVVLVGVLGLLLLTILVLAMWKVGFFKRNRP PLEEDDEE-----GE----- αIIb  
 948 TTNVTWGIQPAPMPVPVWV IILAVLAGLLLLAVLVFVMYRMGFFKRV RPPQEE-QEREQ---LQPHENGE GNSSET αV

Fig. S1a\_p2



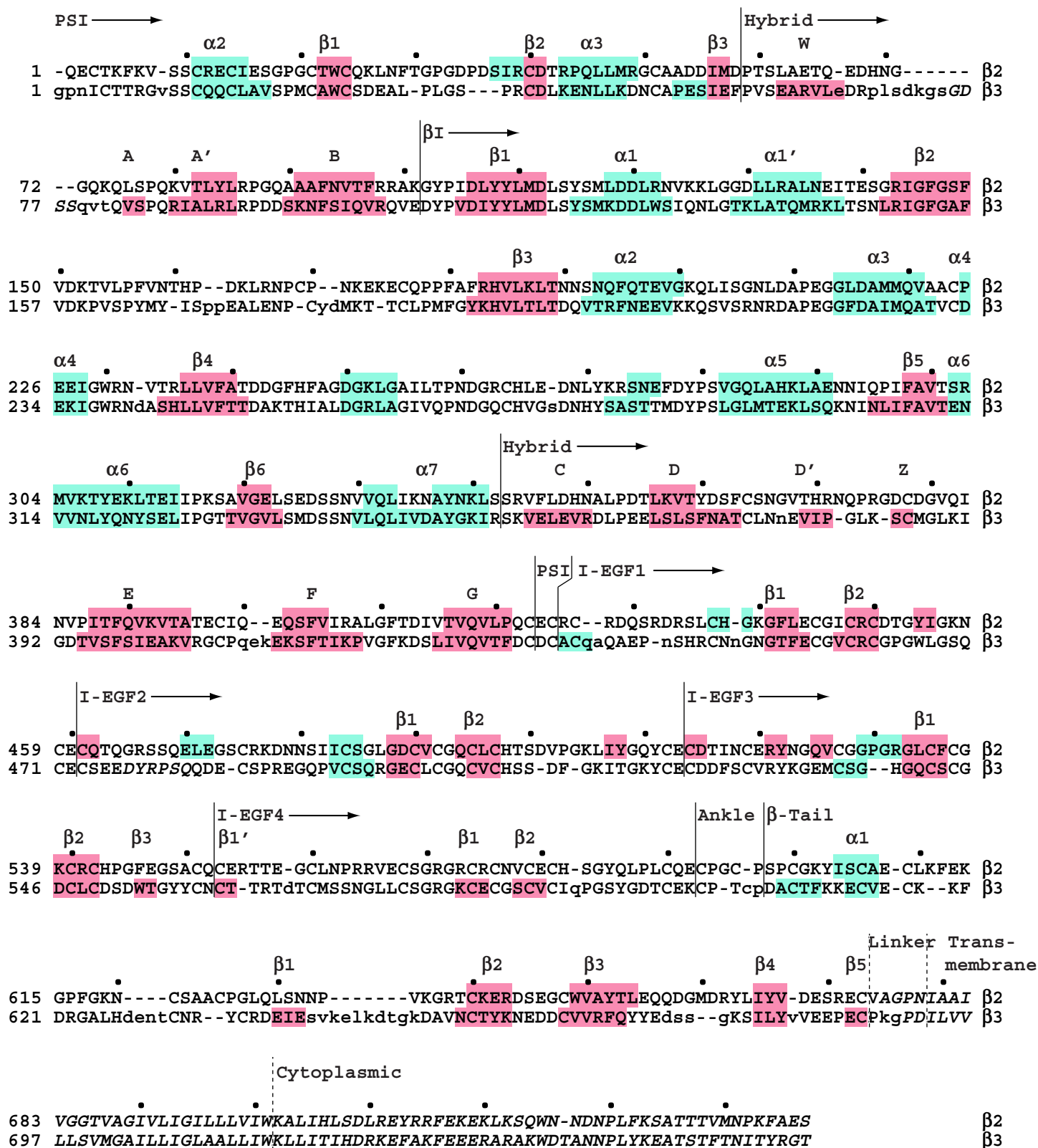
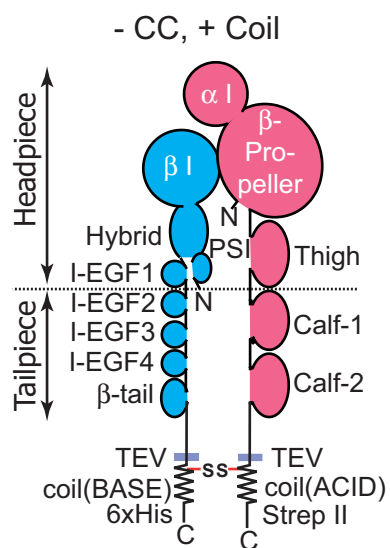


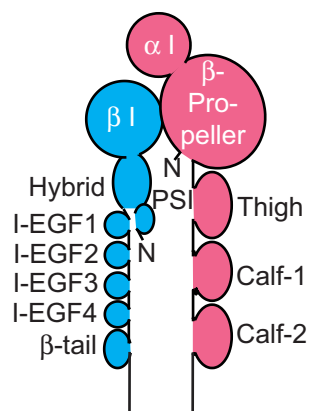
Fig. S1b

a

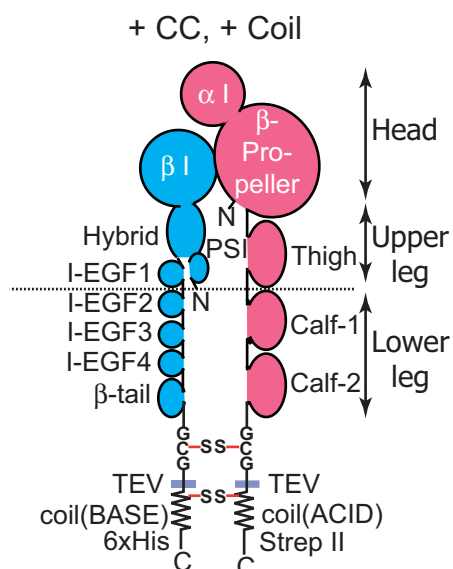


TEV

- CC, - Coil



b



TEV

+ CC, - Coil

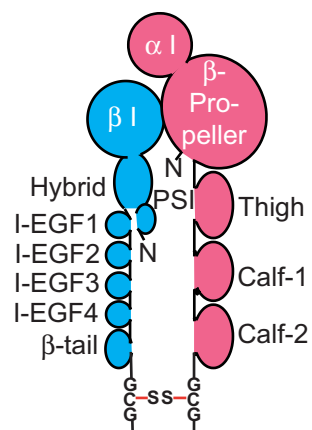
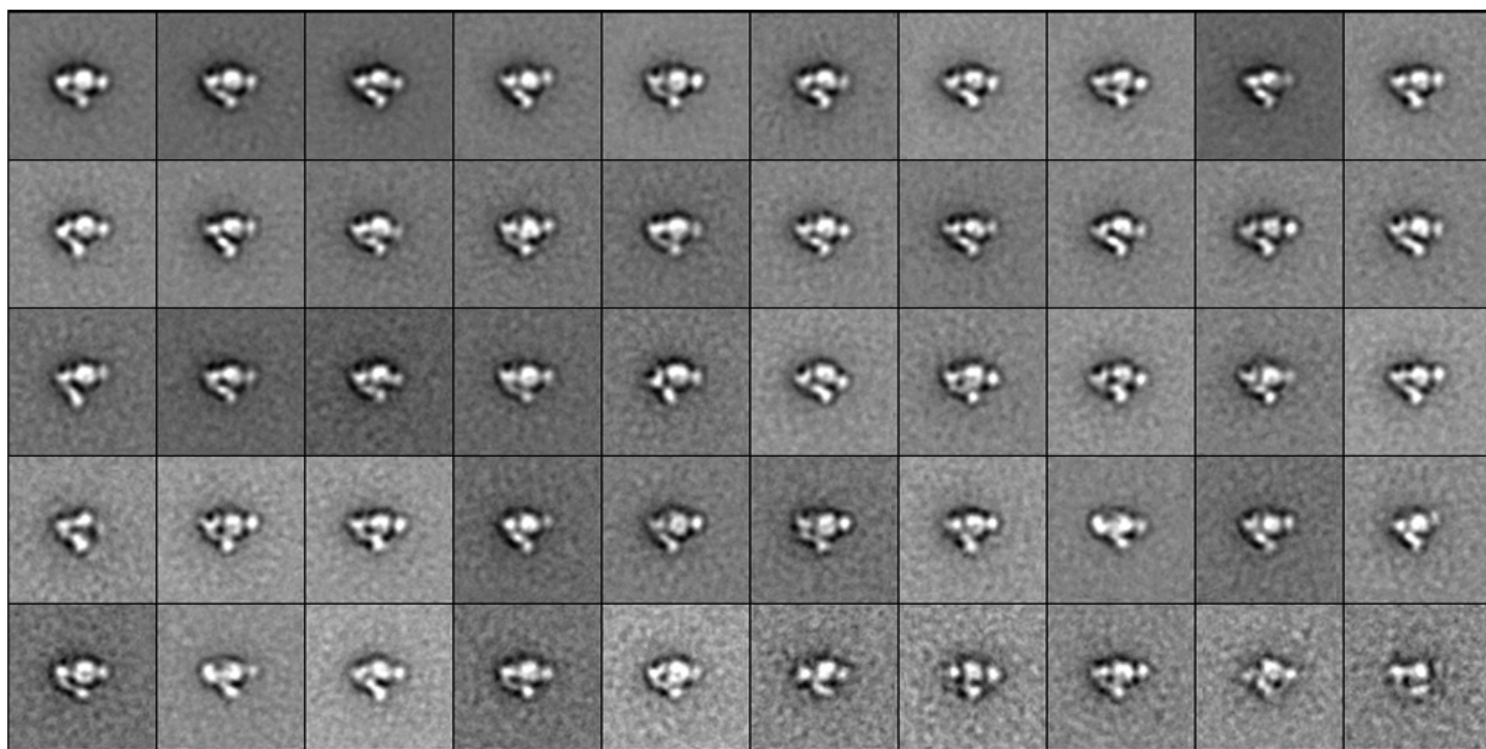


Fig. S2a, b

**c**

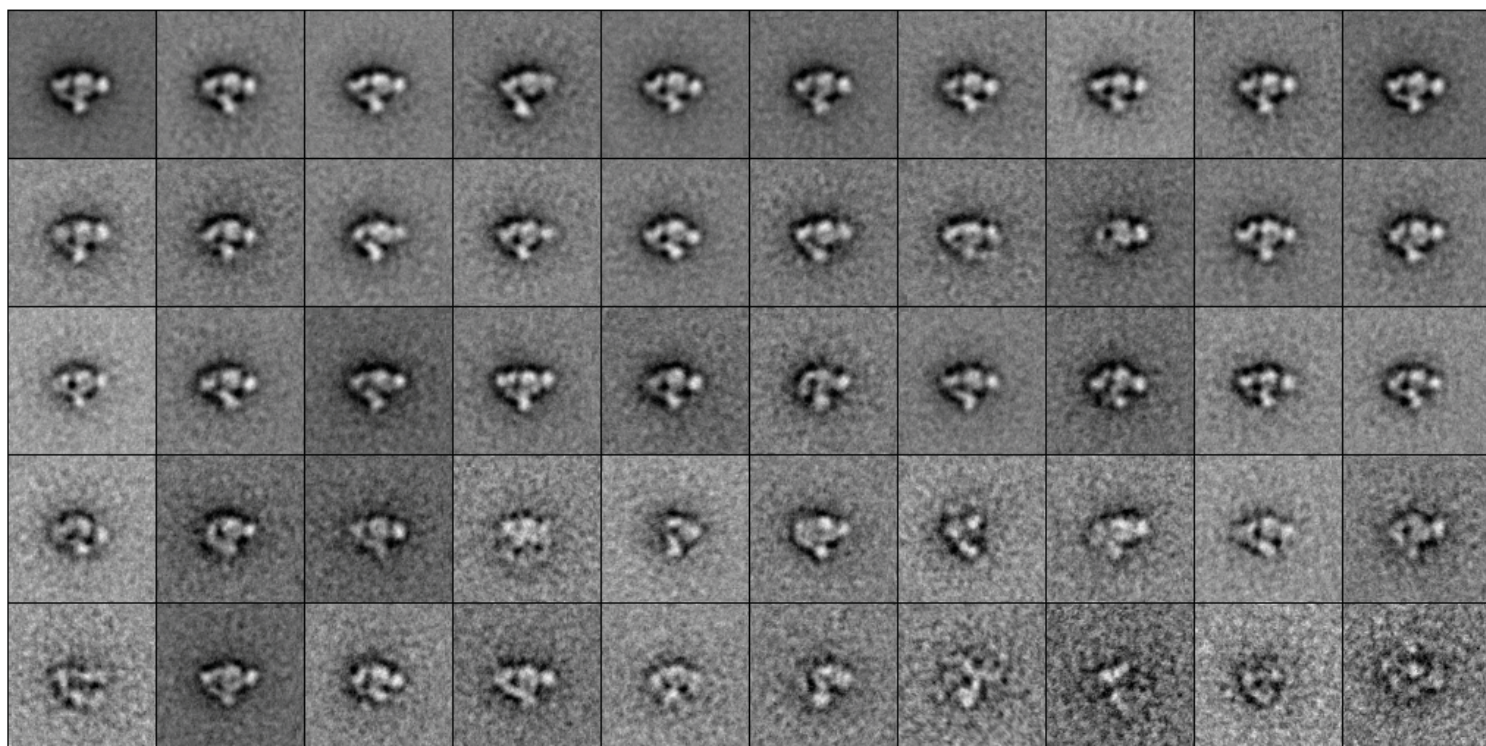
Class average of  $\alpha_x\beta_2$  (+ CC, + Coil)



20 nm

**d**

Class average of  $\alpha_x\beta_2$  (– CC, + Coil)



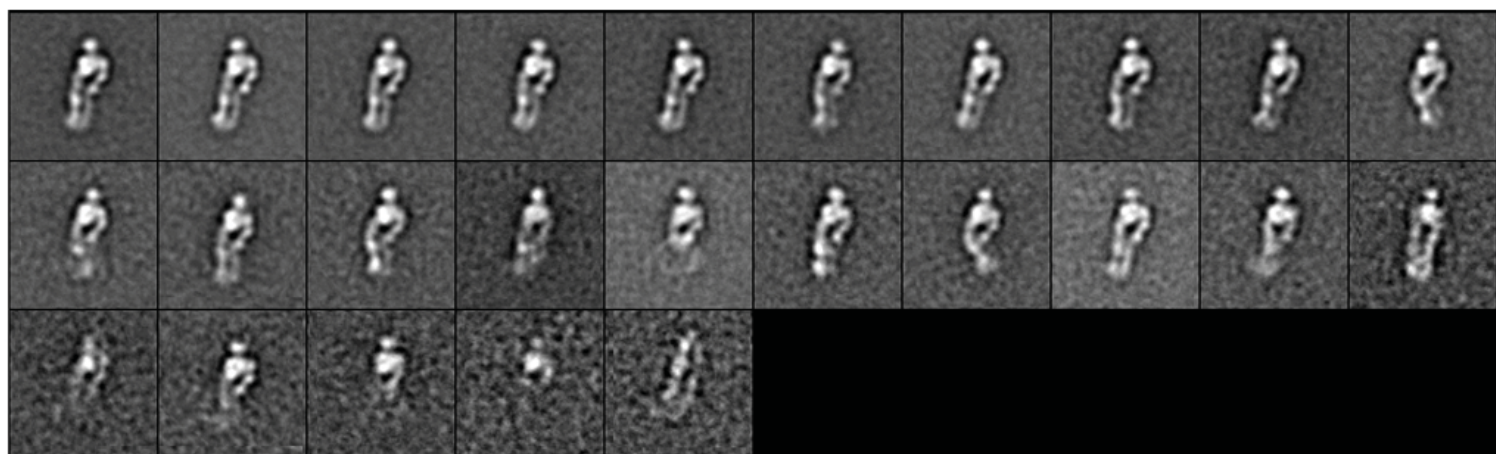
20 nm

Fig. S2c, d

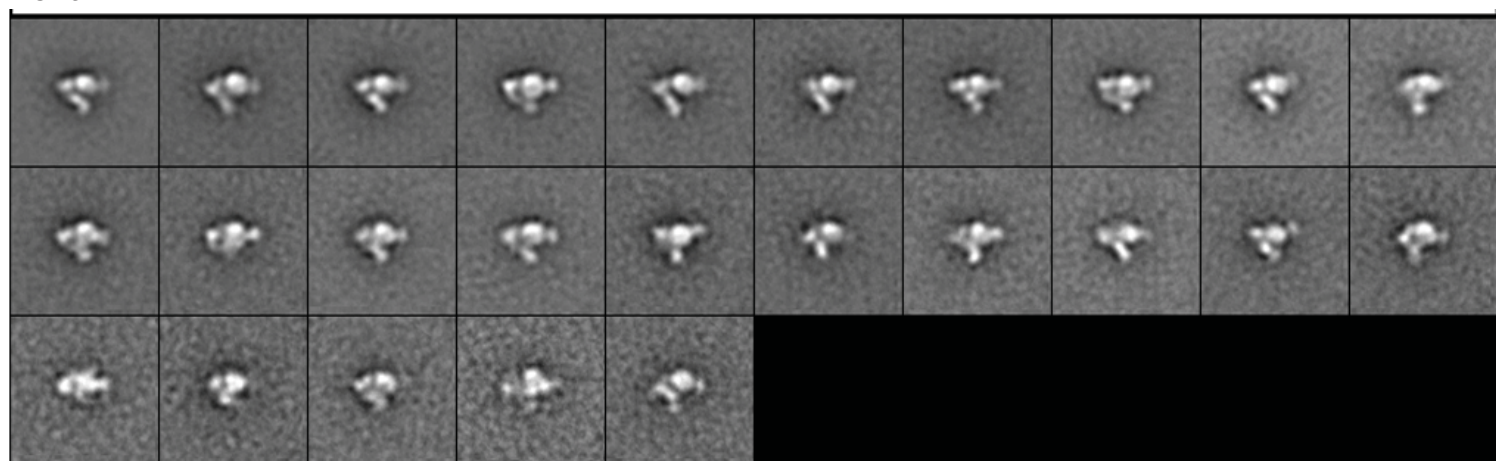


**e** Class average of  $\alpha_x\beta_2$  (+ CC, – Coil), segregated into extended and bent groups

Extended



Bent



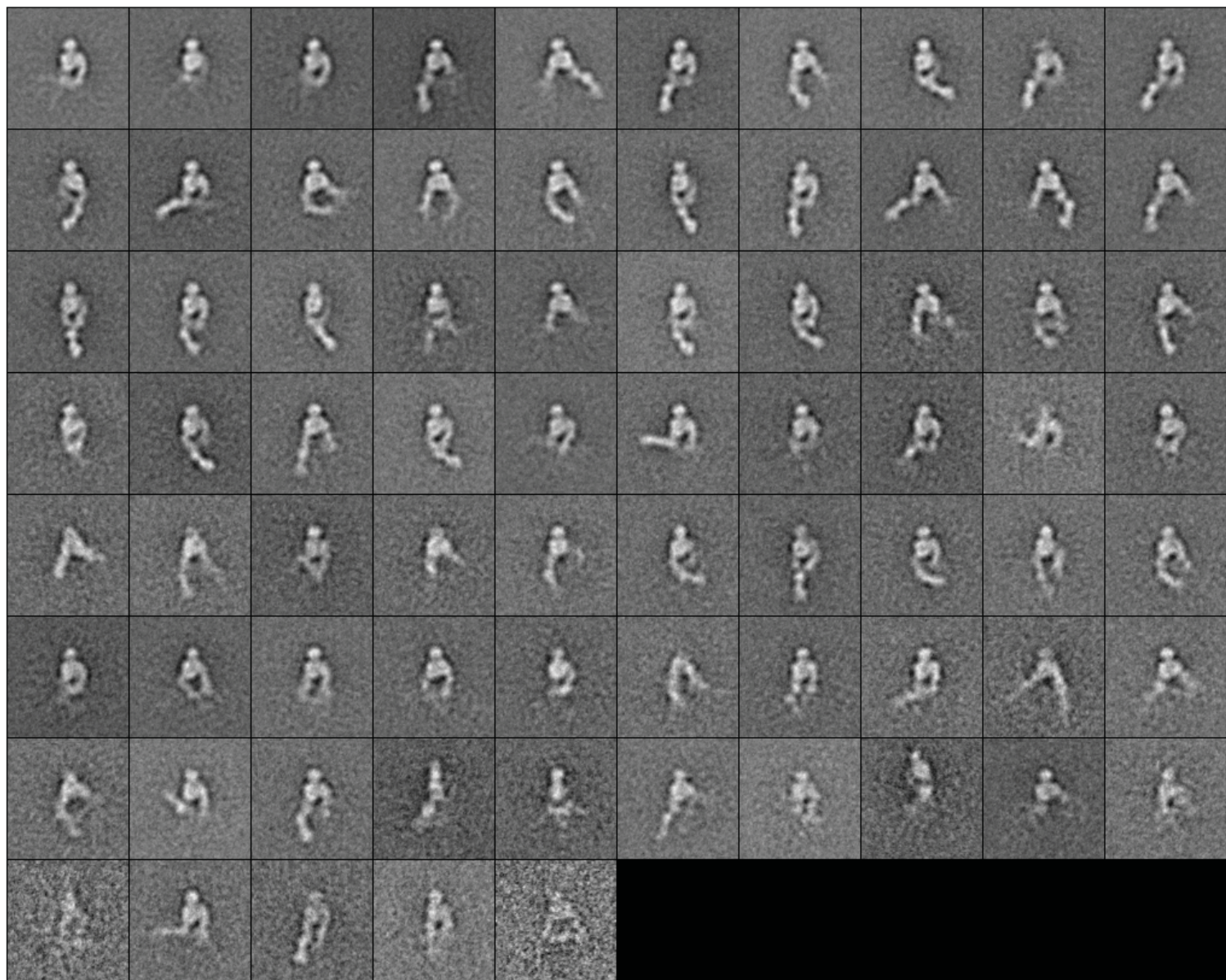
20 nm



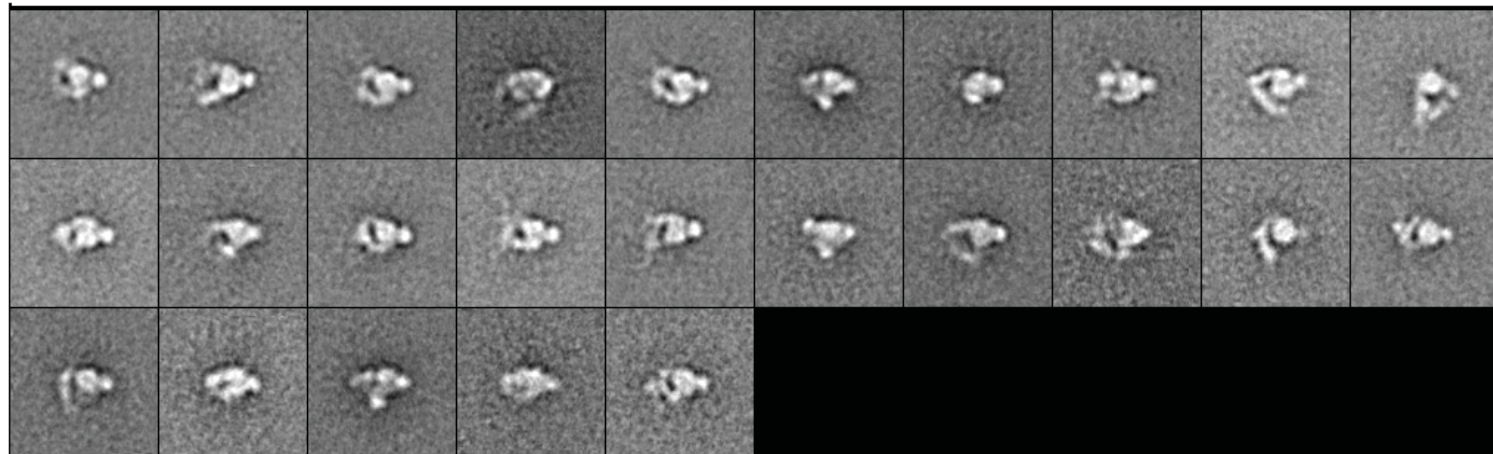
Fig. S2e



**f** Class average of  $\alpha_x\beta_2$  ( – CC, – Coil ), segregated into extended and bent groups  
 Extended



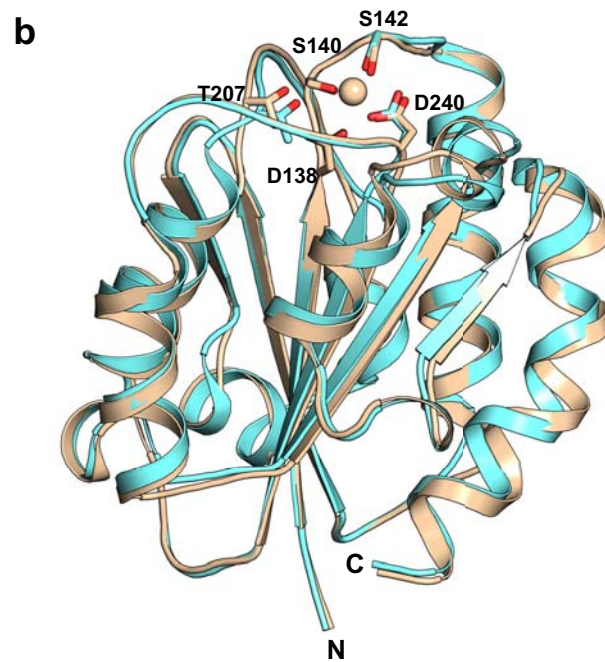
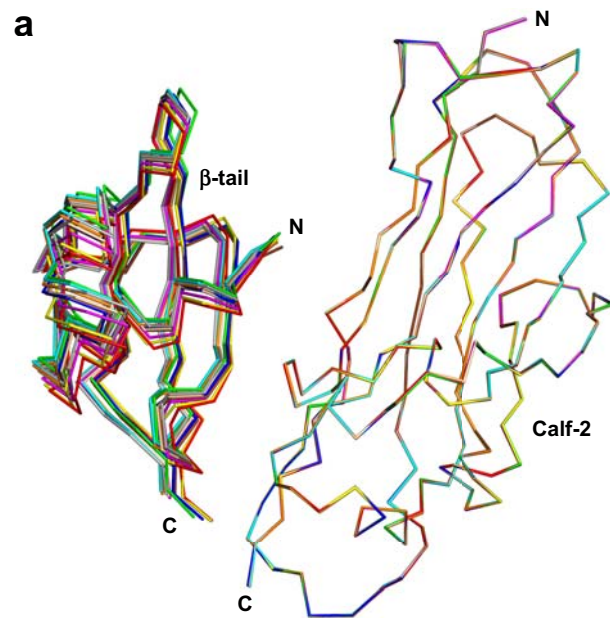
Bent



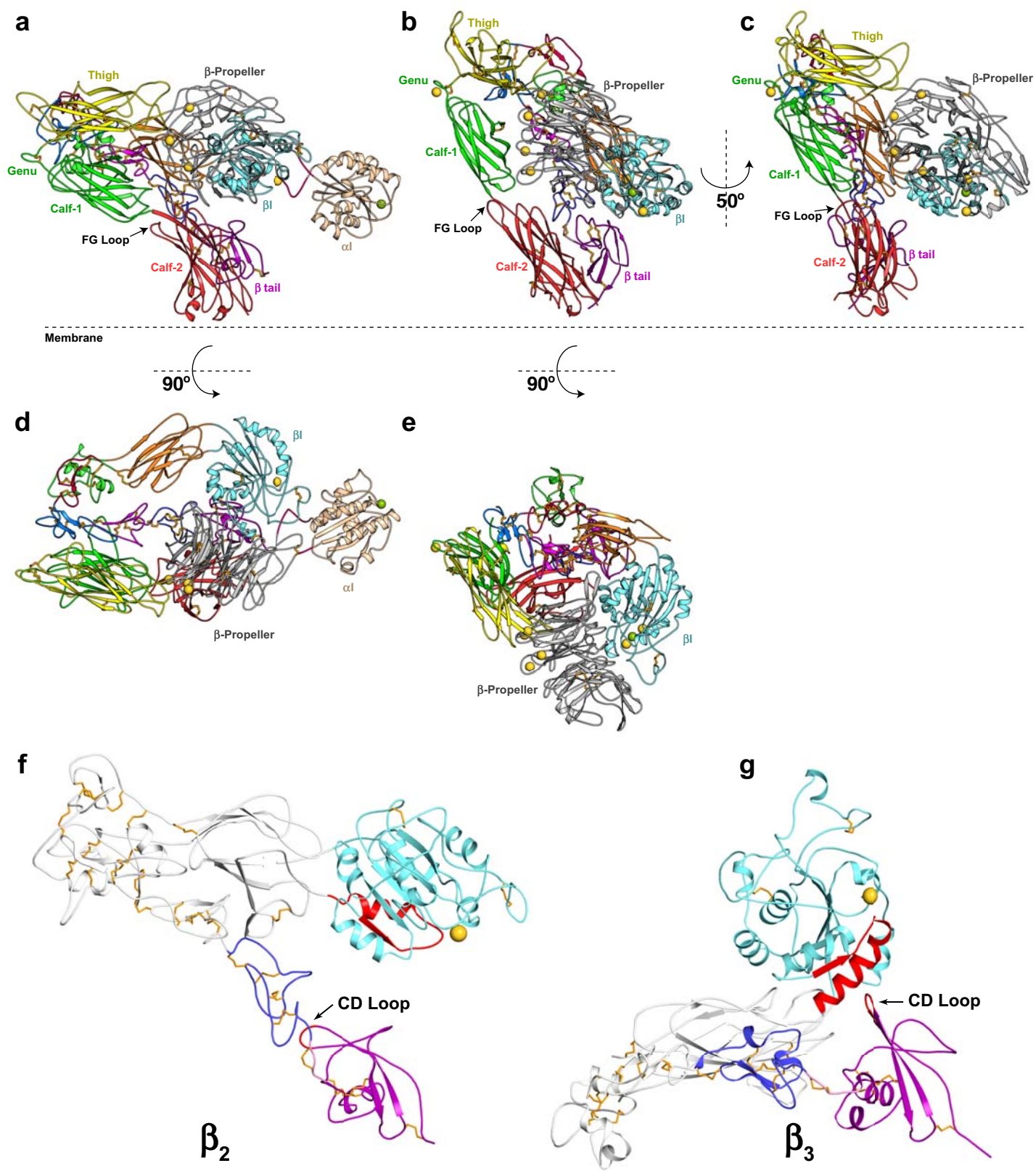
20 nm

Fig. S2f





**Fig. S3**



**Fig. S4**


**a**

	Thigh	Genu	Calf-1		
$\alpha$ integrins	$\alpha$ X	YFTASLPFEK-NCGADHICQDNLGIS-FSFPG	770		
	$\alpha$ D	LFTASLPFEK-NCGQDGLCEGDLGVT-LSFSG	769		
	$\alpha$ M	LFTALFPFEK-NCGNDNICQDDLSIT-FSFMS	772		
	$\alpha$ L	SETWEIPFEK-NCGEDKKCEANLRVS-FSPAR	764		
	$\alpha$ E	FAIFQLPYEK-ACKNKLFCVAELQLA-TTVS-	821		
	$\alpha$ 1	SVHEYIPFAK-DCGNKEKCISDLSLH-VATTE	798		
	$\alpha$ 2	AKVFSIPFHK-DCGEDGLCISDLVLD-VRQIP	778		
	$\alpha$ 10	SIQKLVPFSK-DCGPDNECVTDLVLD-VNMDI	785		
	$\alpha$ 11	TLRVSVPFWN-GCNEDEHCVPDLVLD-ARSDL	777		
$\alpha$ -less integrins	$\alpha$ IIb	HVQEQTTRIVL-DCGEDDVCPQLQLT-ASVT-	619		
	$\alpha$ V	NISRQAHILL-DCGEDNVCKPKLEVS-VDSD-	613		RGD binding integrins
	$\alpha$ 8	IVSEQAHILV-DCGEDNLCVPDLKLS-ARPD-	620		
	$\alpha$ 5	RIEDKAQILL-DCGEDNICVPDLQLE-VFGE-	621		
	$\alpha$ 4	IMKKTINFAR-FCAHEN-CSADLQVS-AKIGF	606		Fibronectin binding integrins
	$\alpha$ 9	AQKNQTVFER-NCRSED-CAADLQLQ-GKLLL	608		
	$\alpha$ 3	ENHTEVQFQK-ECGPDNKCESNLQMR-AAFVS	601		
	$\alpha$ 6	TAHIDVHFLKEGCGDDNVCNSNLKLE-YKFACT	621		Laminin binding integrins
	$\alpha$ 7	TQRAEIHFLKQGCGEDKICQSNLQLVHARFCT	623		

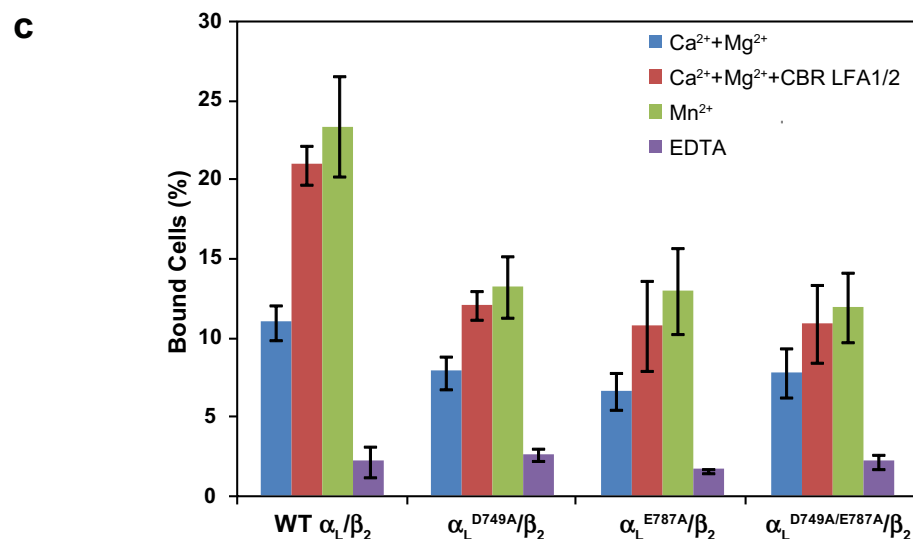
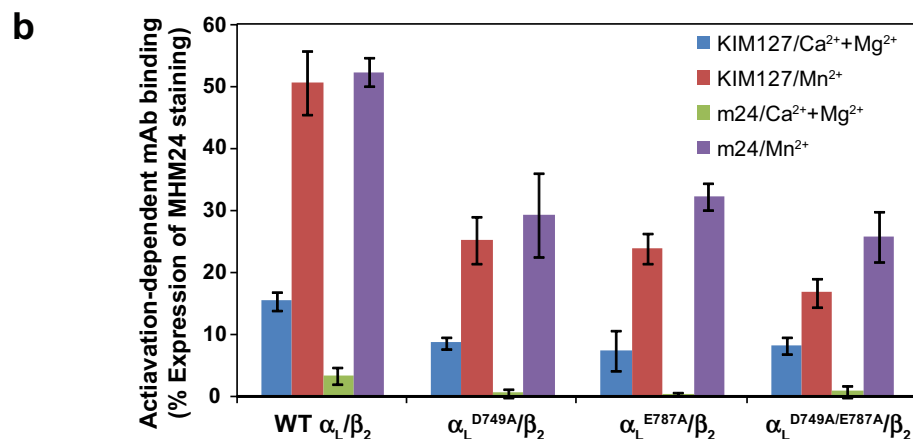


**Fig. S5**

**a**

	$\alpha$ I	C-linker	$\beta$ -Propeller	
				
$\alpha$ X	FDALKDIQNQLKEKIFAIE	EGTETTSSSSFELEMAQEGFS	338	
$\alpha$ D	FAALGSIQKQLQEKIYAVE	GTQSRASSSFQHEMSQEGFS	339	
$\alpha$ M	FEALKTIQNQLREKIFAIE	GTQTGSSSSFEHEMSQEGFS	340	
$\alpha$ L	FEKLKDLFTTELQKKIYVIE	GTSKQDLTSFNMELSSSGIS	330	
$\alpha$ E	YMALDGLLSKLRNYNIISME	GTGTV-GD--ALHYQLAQIGFS	388	
$\alpha$ 1	ELALVTIVKTLGERIFALEA	TADQSAASFEMEMSQTGFS	356	
$\alpha$ 2	EAALLEKAGTLGEQIFSIE	GTVQGGD-NFQMEMSQVGFS	355	
$\alpha$ 10	EAALTDIVDALGDRIFGLE	GSHAENESSFGLEMSQIGFS	356	
$\alpha$ 11	EAALKDIVDALGDRIFSLE	GTNKNET-SFGLEMSQTGFS	350	

**b**

	Calf2	Transmembrane domain
$\alpha$ X	QTTTVLEKYKVHNP	TPLIVGSSIGGLLLLALITAVLY
$\alpha$ M	QTETKVEPFEPNPL	PLIVGSSVGGLLLLALITAALY
$\alpha$ D	QMEMVLEEDEVYNAI	PIIMGSSVGALLLLLALITATLY
$\alpha$ L	VVMKVDVVYEKQ-	MLYLYVLSGIGGLLLLLLIFIVLY

**Fig. S6**

**Upper Ring**

**Lower Ring**

$\alpha_x\beta_2$   
 $\alpha_v\beta_3$   
 $\alpha_{IIIb}\beta_3$

W110  
 L75  
 S72  
 W93  
 F337  
 F171  
 F159  
 Y385  
 Y221  
 Y234  
 Y388  
 Y224  
 Y237  
 Y438  
 Y288  
 Y275  
 A441  
 H291  
 F278  
 $\beta_3$  R261  
 $\beta_2$  K252  
 $\beta_3$  R261  
 F21  
 F21  
 D20  
 Q18  
 Y18  
 Q567  
 F419  
 Y406  
 A416  
 S403  
 Y564

**Fig. S7**